JGR Biogeosciences

RESEARCH ARTICLE
10.1029/2024JG008421

# Mapping Soil Organic Matter, Total Carbon, and Total Nitrogen in Salt Marshes Using UAS-Based Hyperspectral Imaging

**Nayma Binte Nur[1,2], Charles M. Bachmann[1], Anna Christina Tyler[3], Avery Miller[3], Sayem Khan[4], Kimberly E. Union[5,6], Wendy A. Owens-Rios[3,7], Timothy D. Bauch[1], and Christopher S. Lapszynski[1]**

[1]Rochester Institute of Technology, Chester F. Carlson Center for Imaging Science, Rochester, NY, USA, [2]Now at Jet Propulsion Laboratory, California Institute of Technology, Pasadena, CA, USA, [3]Thomas H. Gosnell School of Life Sciences, Rochester Institute of Technology, Rochester, NY, USA, [4]Department of Computer Science and Engineering, University at Buffalo, Buffalo, NY, USA, [5]Department of Environmental Studies, New York University, New York, NY, USA, [6]Now at Department of Environmental Sciences, University of Virginia, Charlottesville, VA, USA, [7]Now at Department of Biology, SUNY Geneseo, Geneseo, NY, USA

**Key Points:**

- Unmanned aerial systems hyperspectral imagery accurately assesses wetland soil properties: soil organic matter (SOM), total carbon (C), and total nitrogen (N)
- Hybrid modeling using elastic net regression and gradient-boosted regression trees enhances prediction accuracy for SOM, C, and N

**Supporting Information:**

Supporting Information may be found in the online version of this article.

**Correspondence to:**

N. B. Nur and C. M. Bachmann,
nn6721@rit.edu;
nayma.binte.nur@jpl.nasa.gov;
cmbpci@rit.edu

**Citation:**

Nur, N. B., Bachmann, C. M., Tyler, A. C., Miller, A., Khan, S., Union, K. E., et al. (2025). Mapping soil organic matter, total carbon, and total nitrogen in salt marshes using UAS-based hyperspectral imaging. *Journal of Geophysical Research: Biogeosciences*, *130*, e2024JG008421. https://doi.org/10.1029/2024JG008421

Received 20 AUG 2024
Accepted 14 MAY 2025



**Abstract** Wetland ecosystems are critical to global carbon and nitrogen cycles. This study leverages unmanned aerial system (UAS)-based hyperspectral imaging to quantify soil organic matter (SOM), total carbon (C), and total nitrogen (N) in moderately to densely vegetated salt marshes at the Virginia Coast Reserve Long-Term Ecological Research (VCR-LTER) site. We utilized elastic net (ENet) regression and gradient-boosted regression trees (GBRT) within a hybrid modeling framework to predict these soil properties using features from the visible to near-infrared (VNIR) and shortwave infrared (SWIR) spectral ranges. Validated through a 1,000-iteration bootstrap analysis, the hybrid model demonstrated robust predictive capabilities. The model achieved mean normalized root mean square error of 0.118 for SOM, 0.127 for C, and 0.138 for N, with corresponding mean $R^2$ values of 0.874, 0.865, and 0.822, respectively. These outcomes highlight the efficacy of integrating advanced statistical methods with high-resolution remote sensing data to enhance soil property estimation in ecologically sensitive areas.

**Plain Language Summary** Wetlands play a pivotal role in our planet's health by absorbing carbon dioxide, a greenhouse gas in the atmosphere. However, measuring how much carbon, along with other vital nutrients like nitrogen, these areas hold is not straightforward due to their complex landscapes. In our research, we used drones equipped with hyperspectral imaging systems to acquire detailed images of a salt marsh system in the VCR-LTER (Virginia Coast Reserve Long-Term Ecological Research) site on Hog Island. We used this imagery to develop models to estimate the levels of organic matter, total carbon, and total nitrogen in the soil. Our work shows that using hyperspectral imagery from drones is a promising method for assessing the health and nutrient content of wetland soils, offering valuable insights for the conservation of these vital ecosystems.

## 1. Introduction

Wetlands are complex ecosystems crucial to global carbon dynamics, serving as significant carbon sinks and habitats for a diverse array of resident and transient species (Aryal et al., 2014; Jobbágy & Jackson, 2000). However, disturbances or land use changes can rapidly deplete these soil carbon stocks, underscoring the importance of conserving soil organic matter (SOM) in such ecosystems (Aryal et al., 2018). The organic component of wetland soils, primarily SOM, underpins nutrient cycling, soil structure, and overall ecosystem productivity (Aryal et al., 2015; Ashman & Puri, 2013; Karami et al., 2012). Because many salt marshes are nitrogen-limited systems (Tyler et al., 2003; Valiela et al., 1978), even moderate increases in nitrogen availability can significantly stimulate primary production (Tyler et al., 2007), while chronic high nitrogen inputs can alter vegetation communities and degrade marsh habitats (Deegan et al., 2012; Valiela et al., 2023). With the outsized role of wetlands in global carbon sequestration, shoreline protection, and climate regulation, understanding these essential soil parameters is paramount (Goldsmith et al., 2020). Maintaining balanced SOM, total carbon (C), and total nitrogen (N) levels is critical for wetland ecosystem health and soil fertility in agricultural systems, where imbalances can directly affect productivity and sustainability (Datta et al., 2022; Leghari et al., 2016).

Despite significant advances in estimating soil properties, SOM, C, and N are hard to measure accurately in wetland environments due to the impact of vegetation cover, moisture, and spatial heterogeneity. Soil sampling and lab procedures can be time-intensive and costly, rendering large-scale surveys impractical. As an alternative, emerging remote sensing technologies—including optical multispectral/hyperspectral imaging, LiDAR, and microwave sensors—offer the capability to assess soil properties across large areas (Eon & Bachmann, 2021; Nur & Bachmann, 2023). Because of the reciprocal relationships among plant productivity, nutrient availability, decomposition, and soil properties, vegetation spectral features can provide indirect information about those properties. Canopy nitrogen content, for example, is highly correlated with soil nitrogen availability, while vegetation biomass and senescence affect SOM. These couplings require a coupled soil and vegetation spectral properties framework for accurate SOM, C, and N retrieval. Laboratory spectroscopy studies have established strong correlations between soil reflectance and properties like organic carbon, forming the basis for predictive soil mapping (Gomez et al., 2008; Rossel et al., 2006; Shepherd & Walsh, 2002). Building on this foundation, digital soil mapping approaches integrate remote sensing data to predict soil variables across landscapes (McBratney et al., 2003; Minasny & McBratney, 2016). Previous studies have investigated other remote sensing approaches like multispectral satellite remote sensing imagery (Vaudour et al., 2019; Zhou et al., 2021; Žížala et al., 2019), aerial hyperspectral imagery (Bangelesa et al., 2020; Gholizadeh et al., 2018), and laboratory spectrometry (Mahmud et al., 2024; Monsalve et al., 2023) in an effort to quantify soil nitrogen and organic carbon in varying landscape types. While these methods have demonstrated potential, they often rely on either bare soil conditions, controlled laboratory settings, or moderate spatial resolution, which can limit their applicability in complex environments like wetlands.

Recent advancements in airborne and unmanned aerial systems (UAS)-based hyperspectral imaging have demonstrated improved accuracy in mapping soil properties at high spatial resolution. UAS platforms provide flexible, high-resolution data collection and have been applied in a wide range of domains, including precision agriculture (Ezenne et al., 2019; Hunt et al., 2014; Saif et al., 2023), environmental and vegetation monitoring (Palace et al., 2018; Shafian et al., 2018), land restoration and mining surveys (Padró et al., 2019), and urban infrastructure inspection (Rakha & Gorodetsky, 2018; Shukla & Karki, 2016), among others (Chahl, 2015). Hyperspectral sensors capture continuous, narrow spectral bands, providing more detailed spectral information than traditional multispectral sensors, making them highly effective for a wide range of scientific and technological applications (Chaity & van Aardt, 2024; Smith et al., 2023). This rich spectral detail improves the ability to discriminate near-surface soil properties with complex reflectance characteristics, enhancing the mapping of SOM, C, and N (Castaldi et al., 2016; Gholizadeh et al., 2018; Sun et al., 2022). Recent studies using hyperspectral data coupled with machine learning algorithms have reported high accuracy in predicting soil organic carbon and N (Bao et al., 2021; Zhou et al., 2021), affirming the advantage of hyperspectral imaging for soil assessments.

However, soil surface factors such as moisture, roughness, vegetation cover, and spectral mixing can introduce uncertainties in remote sensing-derived soil properties. These confounding effects are particularly problematic in wetland environments, where vegetation, hydrology, and soil conditions change dynamically (Van Wesemael et al., 2021; Vaudour et al., 2019; Xu et al., 2023; Yang et al., 2021). Our study addresses these challenges by leveraging UAS-based hyperspectral imaging in salt marshes and developing a hybrid modeling approach that integrates elastic net (ENet) regression with gradient-boosted regression trees (GBRT). This combined model captures linear and nonlinear relationships in spectral data, improving the accuracy of SOM, C, and N predictions. Unlike previous remote sensing approaches primarily focused on bare soil or agricultural settings, our study applies hyperspectral imaging in a vegetated wetland environment, demonstrating high-accuracy retrieval of soil properties despite vegetation interference. By combining VNIR-SWIR hyperspectral imagery having high spatial resolution with a robust hybrid modeling methodology, this study demonstrates a new approach to improve monitoring of wetland soil from remote sensing. Specifically, this study illustrates a new way to more effectively map wetland carbon and nutrients, which are critical to wetland conservation and climate change adaptation.

## 2. Study Framework and Data Collection

### 2.1. Study Area and Site Description

During our field campaigns on Hog Island, part of the Virginia Coast Reserve Long-Term Ecological Research (VCR-LTER) site on the Delmarva Peninsula's Atlantic coast (Virginia Coast Reserve Long-Term Ecological

Research, 2025), in 2019, we collected ground truth data and captured hyperspectral imagery from UAS. Situated at 37° 25' 5.91" north and 75° 41' 36.71" west approximately 14 km from the Peninsula, Hog Island is a barrier island extending 10 km in length and 2.5 km in maximum width. Managed by The Nature Conservancy, Hog Island has been mostly uninhabited since the middle of the 20th century. This seclusion has made it an ideal location for conducting significant research in ecology and geology (C. M. Bachmann et al., 2002; C. M. Bachmann et al., 2003; C. Bachmann et al., 2021; Goldsmith et al., 2020; Eon et al., 2019; McLoughlin et al., 2015; Nur & Bachmann, 2023; Nur, Bachmann, & Bauch, 2023; Nur, Miller, et al., 2023; Osgood & Zieman, 1993; Tyler & Zieman, 1999; Tyler et al., 2003; Young et al., 2007). The island's shallow coastal lagoon, Hog Island Bay, borders it to the west, with the Atlantic Ocean to the east (Hayden et al., 1991). *Spartina alterniflora*, the dominant macrophyte, forms classic zonation patterns along the lagoonal shore of the island, with tall-form plants in the low marsh and short-form plants in the mid and high zones (Bortolus et al., 2019; Valiela et al., 1978). In 1962, a powerful nor'easter deposited nearly 1 m of sand on the island's southern end, burying the preexisting marsh and raising the intertidal platform (Stewart, 1962). Following the recolonization of vegetation at different times across the overwash fan, a chronosequence of marshes with varying ages emerged (Tyler & Zieman, 1999; Walsh, 1998). The ages of the marshes were identified from the time of the initial appearance of *Spartina alterniflora* in aerial images. The oldest marsh can be traced back to at least 1850, while the most recent one was established in 2011. In our field campaign, we investigated marshes ranging in age from 8 to at least 170 years. These marshes experience erosion and expansion and are marked by areas of marsh die-off. The heterogeneity in marsh age and condition renders this site ideal for assessing soil properties within an environment where spatial heterogeneity occurs across smaller spatial scales. In July 2019, we conducted a major field campaign to characterize and map the marsh chronosequence on Hog Island, primarily focusing on the low to midmarsh zones. This study focuses on two chronosequence sites: the mature marsh site from 1850, also known as Broadwater, and the young marsh site consisting of marshes established between 1989 and 2011 (see Figure 1).

### 2.2. Instrumentation and Data Calibration

We employed two multisensor payloads on the MX1 platform mounted on a DJI Matrice 600 (Kaputa et al., 2019) for the 2019 field campaign. The primary payload comprised a visible and near-infrared (VNIR) hyperspectral imager, a LiDAR, a thermal imager, and a high-resolution RGB imager. The second payload consisted of a shortwave infrared (SWIR) hyperspectral imaging sensor. This study analyzed hyperspectral images captured by the Headwall Nano (VNIR range) and Headwall Micro SWIR (SWIR range) imaging sensors onboard the UAS (C. Bachmann et al., 2021; Eon & Bachmann, 2021; Lee et al., 2024; Nur et al., 2022; Nur & Bachmann, 2023; Nur, Miller, et al., 2023; Nur, Bachmann, & Bauch, 2023; Saif et al., 2023). The flights were conducted at 50-m altitude with an average speed of 2.5 m/s. Flight duration for each sortie was approximately 12–15 min due to battery constraints.

The Headwall Nano images in the VNIR, covering this spectral range with 270 spectral bands from 0.4 to 1 μm. At the altitude flown by the UAS platforms in this study, the spatial resolution of the Nano VNIR imagery was 0.056 m in the 640 across-track spatial pixels per scan line. The sensor's 7.4 μm pixel pitch ensures high spatial resolution. The Headwall Nano has a 12-bit analog-to-digital converter (ADC) resolution for accurate spectral representation and a maximum frame rate of 300 Hz for efficient aerial survey data collection.

The Headwall Micro SWIR sensor analyzes the SWIR spectrum with 267 spectral bands from 0.9 to 2.5 μm. At the altitude flown by the UAS in this study, the spatial resolution of the SWIR imagery was 0.05 m in the 384 across-track spatial pixels. The Headwall Micro SWIR captures high-resolution images with a 24 μm pixel pitch. This sensor has 16-bit ADC resolution for SWIR spectral information. The Headwall Micro SWIR also has a maximum frame rate of 240 Hz, allowing for efficient data acquisition during aerial surveys.

In our systematic approach to data calibration, we recorded the ground truth radiance of three Permaflect® calibration panels (light gray, dark gray, and black) and a white Spectralon® plaque using an SVC 1024i spectrometer just before the UAS flights. The Permaflect® calibration panels provided a range of reflectance values, ensuring accurate radiometric correction across different surface brightness levels. These steps were foundational for applying Equation 1 to determine the panels' true reflectance values.

$$R_{panel} = \frac{L_{panel}}{L_{spectralon}} \cdot C_{spectralon} \quad (1)$$

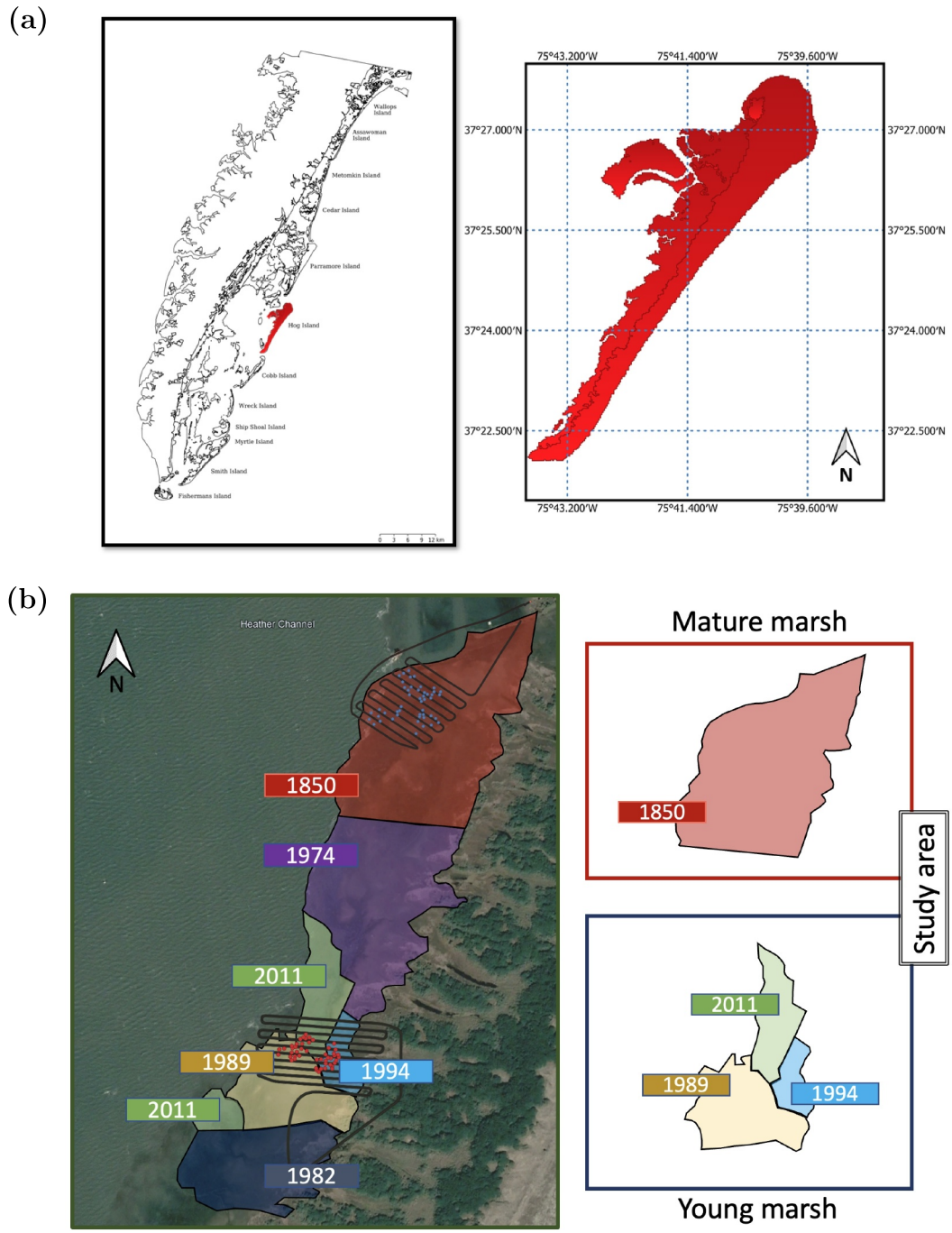


**Figure 1.** Delmarva Peninsula and Hog Island site map with marsh ages. Hog Island in the Delmarva Peninsula, Virginia, includes barrier islands, estuaries, and shallow bays of the Virginia Coast Reserve Long-Term Ecological Research site. (a) An overall site map of the region (Virginia Coast Reserve Long-Term Ecological Research, 2025), with Hog Island marked in red. (b) Individual marsh ages delineated by vegetation onset years (left) and the mature and young marsh study areas (right). The red dots represent our sample locations in young marshes, while the blue dots indicate our sample locations in mature marshes. UAS flight lines are overlaid in black.

where, $R_{panel}$ represents the reflectance of the calibration panel, $L_{panel}$ denotes the radiance recorded from the calibration panel, $L_{spectralon}$ is the radiance from the Spectralon® plaque, and $C_{spectralon}$ is the Spectralon® plaque's calibration coefficient.

In the field, the independently operated UAS-mounted Nano and SWIR sensors captured hyperspectral imagery that we orthorectified and converted into radiance data using Headwall's Hyperspec III SpectralView software (Hyperspectral and Operational Software, 2024). To achieve georeferencing correctly, the drones were equipped with high-accuracy Applanix GPS/IMU units that provided accurate metadata for yaw, pitch, and roll. These metadata were included in the data processing stream and geometric registration of the hyperspectral data. Additionally, real-time kinematic ground control point corrections, using AeroPoints placed inside the scene, were acquired with a Trimble GPS, which accurately geolocated them. These corrections enhanced geodetic coordinate alignment, reducing spatial error and improving overall geolocation accuracy. To ensure spatial alignment between different imaging modalities, we applied postprocessing coregistration techniques, including feature matching and image alignment, before layer stacking the VNIR and SWIR imagery. These steps helped minimize spatial discrepancies caused by differences in acquisition platforms and sensor perspectives. We extracted the spectra of each calibration panel with the ENVI software (NV5 ENVI 6.0, 2024). We used the empirical line method within the same software (ENVI: Atmospheric Correction via Empirical Line Method, 2024) to establish a correlation between the Permaflect® panels' ground truth reflectance and the UAS-acquired radiance spectra. This approach enabled us to convert the radiance to reflectance for each wavelength. Our thorough calibration protocol assures that the reflectance data derived from radiance measurements are consistent and comparable, offering resilience against variations in data acquisition date, sensor type, and environmental conditions. This process ensures the data integrity for both the Nano and SWIR hyperspectral imaging systems.

Figure 2 presents the reflectance spectra from the UAS hyperspectral imagery across various wavelengths for each plot where we collected ground truth data. While the spectra are influenced by SOM, C, and N percentages, other factors such as vegetation cover, soil moisture, surface roughness, and mineral composition also contribute to spectral variations. To enhance the quality of the hyperspectral reflectance data obtained from UAS, we applied a Savitzky-Golay filter (Savitzky & Golay, 1964; Schafer, 2011). This smoothing technique was employed to reduce noise while preserving the spectral shape and features essential for accurate soil property estimation. The Savitzky-Golay filter, a polynomial smoothing method, was chosen for its effectiveness in maintaining high-resolution spectral information, which is critical in distinguishing subtle variations in soil properties. The parameters selected for the Savitzky-Golay filter, including the polynomial order and window size, were determined based on preliminary tests to optimize the balance between noise reduction and spectral fidelity. Noise levels were generally consistent across flight lines, with some variation due to environmental factors such as illumination conditions and sensor-specific artifacts. While no systematic bias was observed, slight signal-to-noise ratio (SNR) variations were noted in certain spectral regions, particularly at the edges of the VNIR and SWIR bands. These discrepancies were avoided by applying a Savitzky-Golay filter for spectral smoothing to the spectral data. After correction, the Spectralon and calibration panel spectra matched anticipated reflectance curves, confirming the calibration process. This preprocessing step was instrumental in ensuring that subsequent analyses, including the development of predictive models, were based on high-quality data, thereby enhancing the reliability of our findings.

### 2.3. Ground Truth Data Collection

Ground truth data collection was essential for validating our UAS hyperspectral imagery analysis. In this study, we used 96 sample plots, 55 in the young marsh and 41 in the mature marsh. For each 0.25 $m^2$ plot, sediment cores were collected to evaluate SOM, C, and N. The sediment was first dried and then homogenized using a mortar and pestle. The percentage of soil organic matter (%SOM) was assessed for a subsample using the loss on ignition method (Heiri et al., 2001). An additional 25 mg of sediment was used for analysis of total carbon (%C) and total nitrogen (%N) content using a Perkin Elmer 2,400 elemental analyzer. All analyses were conducted in duplicate.

## 3. Model Development and Implementation

This section provides an overview of the comprehensive workflow adopted in this study, as shown in Figure 4. The flowchart illustrates each step of our methodology, from data acquisition and preprocessing to model development and performance evaluation, highlighting the systematic and interconnected phases of our research.

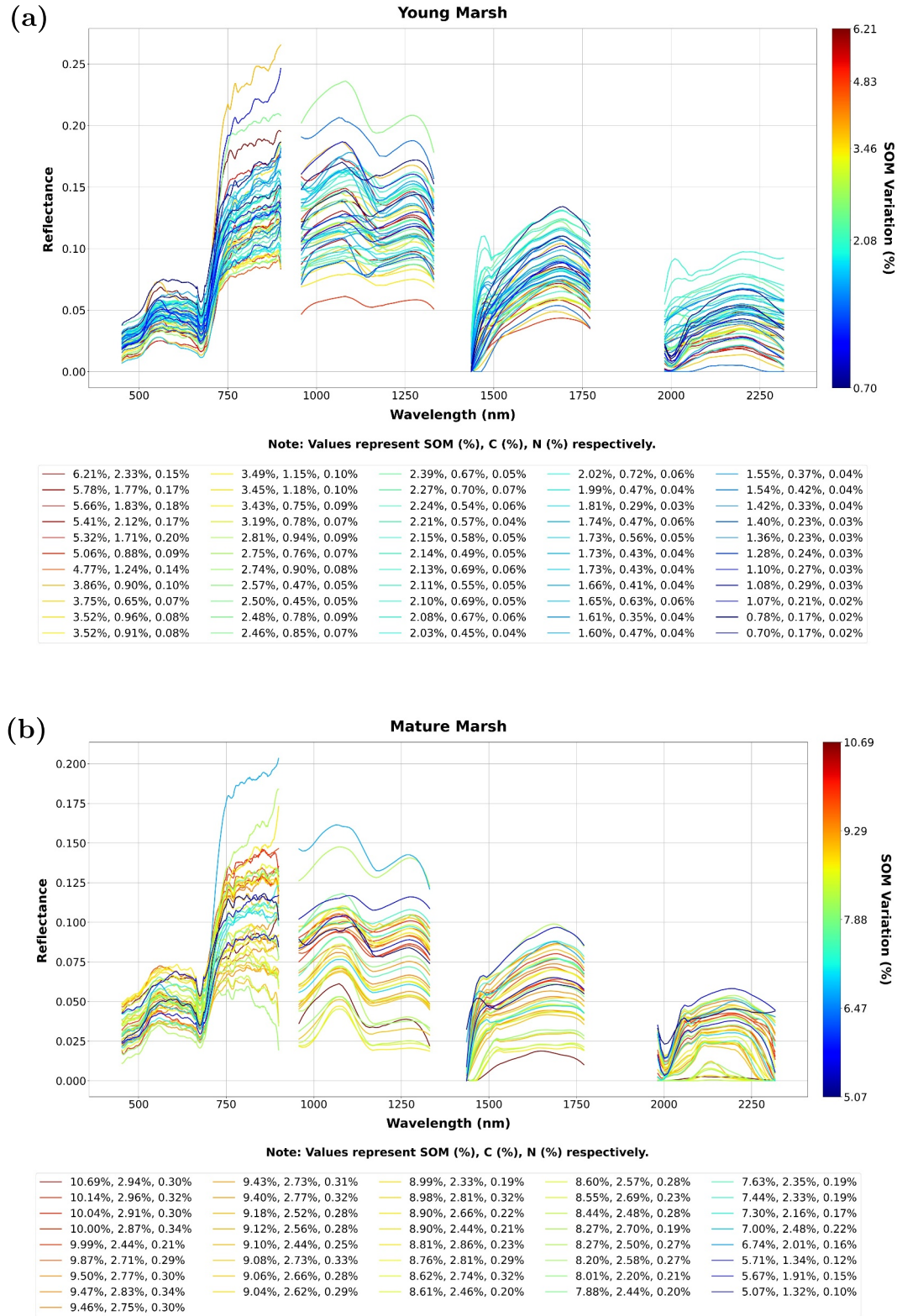


**Figure 2.** Reflectance spectra of (a) young marsh and (b) mature marsh, with colors indicating soil organic matter (SOM) percentage variation. Data were smoothed using a Savitzky-Golay filter (Savitzky & Golay, 1964). The color bar represents SOM variation, while SOM, total carbon, and total nitrogen percentages for each sample are labeled below the plots.

### 3.1. Characterization and Correlation of Input Features

We stacked the VNIR and shortwave infrared (SWIR) images using ENVI software to create a comprehensive spectral data set, following geometric correction to account for different acquisition platforms (NV5 ENVI 6.0, 2024). The VNIR range (400–1,000 nm) provided critical information on vegetation health, chlorophyll content, and surface characteristics, while the SWIR range (1,000–2,500 nm) offered insights into water content, soil properties, and vegetation stress, together allowing us to analyze the biophysical and biochemical characteristics of surface materials comprehensively. We utilized a linear spectral unmixing algorithm to derive the soil and vegetation fractions within each pixel (Figures 3 and 4). End-members were selected based on field observations and spectral analysis for spectral unmixing. A highly vegetated region was chosen as the vegetation end-member, while a bare soil region was used as the soil end-member. Linear spectral unmixing was applied using these two spectra to estimate the fractional cover of vegetation and soil in each pixel.

To further enhance our analysis, we calculated various spectral indices (SIs) that provide targeted information on vegetation health, stress, and productivity (Figure 4). The selected SIs, detailed in Table 1, were chosen for their relevance in capturing specific aspects of vegetation and soil properties, including vegetation health, canopy structure, pigment concentration, and water content. They played a significant role in estimating SOM, C, and N content by providing insights into vegetation greenness and biomass, and thereby carbon sequestration and plant nitrogen content. Similarly, specific indices among the set that we employed in our model are related to water stress and photosynthetic efficiency and proved crucial for understanding soil moisture dynamics and nutrient availability. Figure 3 displays the distribution of vegetation cover and NDVI, a measure of health, across the study area, underscoring the importance of robust feature selection, including SIs and vegetation-soil fractions, in our modeling approach.

There were both linear and nonlinear features in the relationships among SIs and SOM, C and N, as shown in the 3-D plots in Figure 5, highlighting the importance of a comprehensive modeling approach. We utilized elastic net (ENet) (De Mol et al., 2009; Zou & Hastie, 2005) to capture linear relationships, benefiting from its ability to manage multicollinearity and perform feature selection effectively. We employed gradient-boosted regression trees (GBRT) (Friedman, 2001; Natekin & Knoll, 2013) to model nonlinear interactions in order to address the complexities that linear models cannot capture. The subsequent subsection provides detailed descriptions and justifications for these specific modeling techniques.

### 3.2. Detailed Model Architectures

#### 3.2.1. Elastic Net Regression

This study initially applied elastic net (ENet) regression (De Mol et al., 2009; Zou & Hastie, 2005), selected for its robustness in managing our data set, which comprises a limited number of samples but a high dimensionality of features. ENet combines the principles of lasso (L1 norm) and ridge (L2 norm) regression, effectively managing situations where predictors are highly correlated or outnumber observations. The L1 norm induces sparsity by reducing some coefficients to zero, thereby pinpointing the most relevant predictors, while the L2 norm curtails the coefficients' magnitudes, mitigating overfitting risks. This dual mechanism makes ENet particularly suitable for our high-dimensional data, ensuring both model interpretability and robustness.

#### 3.2.2. Gradient-Boosted Regression Trees

Following elastic net, we used gradient-boosted regression trees (GBRT) (Friedman, 2001; Natekin & Knoll, 2013) to capture complex, nonlinear relationships not addressed by the linear model. GBRT constructs a predictive model iteratively, focusing on the residual errors of previous models, a process which enhances overall prediction accuracy by refining the model progressively. By iteratively learning from the errors of previous models, GBRT can capture intricate patterns and adapt more flexibly to the complexities of the data. This method is advantageous for our data set as it allows the model to adapt more dynamically to the complex interdependencies within the SIs and their relationship with reflectance data. We tuned key hyperparameters, such as the number of trees, learning rate, and tree depth, to optimize the model's performance. This is crucial in environments where the relationship dynamics are not purely random but structured in sequential layers of complexity.

**Table 1**
*Spectral Indices Used as Input Features of the Models and Their Descriptions (ENVI: Vegetation Indices, 2024)*

| Index | Equation | Description |
|---|---|---|
| Normalized difference vegetation index (NDVI) | $\frac{(NIR-Red)}{(NIR+Red)}$ | Measures green vegetation health and density (Rouse et al., 1974). |
| Simple ratio index (SRI) | $\frac{NIR}{Red}$ | Indicates vegetation health and density (Birth & McVey, 1968). |
| Enhanced vegetation index (EVI) | $\frac{2.5\times(NIR-Red)}{(NIR+6\times Red-7.5\times Blue+1)}$ | Designed for areas with a high leaf area index (LAI). Minimizes soil and atmospheric effects (Huete et al., 2002). |
| Atmospherically resistant vegetation index (ARVI) | $\frac{R_{800}-[R_{680}-(R_{450}-R_{680})]}{R_{800}+[R_{680}-(R_{450}-R_{680})]}$ | Reduces atmospheric influence. Useful in areas with high aerosol content (Kaufman & Tanre, 1992). |
| Red-edge normalized difference vegetation index (RENDVI) | $\frac{R_{750}-R_{705}}{R_{750}+R_{705}}$ | Sensitive to changes in canopy foliage and senescence (A. Gitelson & Merzlyak et al., 1994; Sims & Gamon, 2002). |
| Modified Red-Edge Normalized Difference Vegetation Index (MRENDVI) | $\frac{R_{750}-R_{705}}{R_{750}+R_{705}-2\times R_{445}}$ | Corrects for leaf reflection. Used in precision agriculture (Datt, 1999; Sims & Gamon, 2002). |
| Sum green index (SGI) | $\frac{\sum_{i=500\text{nm}}^{600\text{nm}} R_i}{N}$ | Detects changes in greenness. Sensitive to small canopy changes (Lobell & Asner, 2004). |
| Vogelmann red-edge index 1 (VREI1) | $\frac{R_{740}}{R_{720}}$ | Sensitive to chlorophyll, canopy leaf area, and water content (Vogelmann et al., 1993). |
| Vogelmann red-edge index 2 (VREI2) | $\frac{R_{734}-R_{747}}{R_{715}+R_{726}}$ | |
| Vogelmann red-edge index 3 (VREI3) | $\frac{R_{734}-R_{747}}{R_{715}+R_{720}}$ | |
| Red-edge position index (REPI) | $\max\left(\frac{dR}{d\lambda}\right)_{690\text{nm}\le\lambda\le740\text{nm}}$ | Sensitive to chlorophyll changes (Curran et al., 1995). |
| Photochemical reflectance index (PRI) | $\frac{R_{531}-R_{570}}{R_{531}+R_{570}}$ | Indicates photosynthetic efficiency (Gamon et al., 1997; Peñuelas et al., 1995). |
| Structure Insensitive Pigment Index (SIPI) | $\frac{R_{800}-R_{445}}{R_{800}-R_{680}}$ | Measures the carotenoid to chlorophyll ratio (Penuelas et al., 1995). |
| Red-green ratio index (RGRI) | $\frac{\sum_{i=600}^{699} R_i}{\sum_{j=500}^{599} R_j}$ | Indicates leaf redness relative to chlorophyll (Gamon & Surfus, 1999). |
| Normalized Difference Nitrogen Index (NDNI) | $\frac{\log\left(\frac{1}{R_{1510}}\right)-\log\left(\frac{1}{R_{1680}}\right)}{\log\left(\frac{1}{R_{1510}}\right)+\log\left(\frac{1}{R_{1680}}\right)}$ | Estimates nitrogen content in canopies (Fourty et al., 1996; Serrano et al., 2002). |
| Normalized difference lignin index (NDLI) | $\frac{\log\left(\frac{1}{R_{1754}}\right)-\log\left(\frac{1}{R_{1680}}\right)}{\log\left(\frac{1}{R_{1754}}\right)+\log\left(\frac{1}{R_{1680}}\right)}$ | Estimates lignin content in canopies (Fourty et al., 1996; Melillo et al., 1982; Serrano et al., 2002). |
| Cellulose absorption index (CAI) | $0.5(R_{2000}+R_{2200})-R_{2100}$ | Indicates dried plant material. Sensitive to cellulose (C. S. Daughtry, 2001; C. Daughtry et al., 2004). |
| Plant senescence reflectance index (PSRI) | $\frac{R_{680}-R_{500}}{R_{750}}$ | Indicates canopy stress and senescence (Merzlyak et al., 1999). |
| Carotenoid Reflectance Index 1 (CRI1) | $\frac{1}{R_{510}}-\frac{1}{R_{550}}$ | Measures the carotenoid to chlorophyll ratio (A. A. Gitelson et al., 2002). |
| Carotenoid Reflectance Index 2 (CRI2) | $\frac{1}{R_{510}}-\frac{1}{R_{700}}$ | Similar to CRI1, but more effective for high carotenoid concentrations (A. A. Gitelson et al., 2002). |
| Anthocyanin Reflectance Index 1 (ARI1) | $\frac{1}{R_{550}}-\frac{1}{R_{700}}$ | Measures anthocyanin content. Indicates stressed vegetation (A. A. Gitelson et al., 2002). |
| Anthocyanin Reflectance Index 2 (ARI2) | $R_{800}\left(\frac{1}{R_{550}}-\frac{1}{R_{700}}\right)$ | Detects higher concentrations of anthocyanins in vegetation (A. A. Gitelson et al., 2001). |
| Water band index (WBI) | $\frac{R_{970}}{R_{900}}$ | Sensitive to canopy water status (Champagne et al., 2001; Peñuelas et al., 1993). |
| Normalized Difference Water Index (NDWI) | $\frac{R_{857}-R_{1241}}{R_{857}+R_{1241}}$ | Sensitive to canopy water content (Gao, 1995; Jackson et al., 2004). |
| Moisture Stress Index (MSI) | $\frac{R_{1599}}{R_{819}}$ | Sensitive to leaf water content. Higher values indicate greater water stress (Ceccato et al., 2001; Hunt Jr & Rock, 1989). |
| Normalized Difference Infrared Index (NDII) | $\frac{R_{819}-R_{1649}}{R_{819}+R_{1649}}$ | Sensitive to water content in canopies (Klemas & Smart, 1983). |

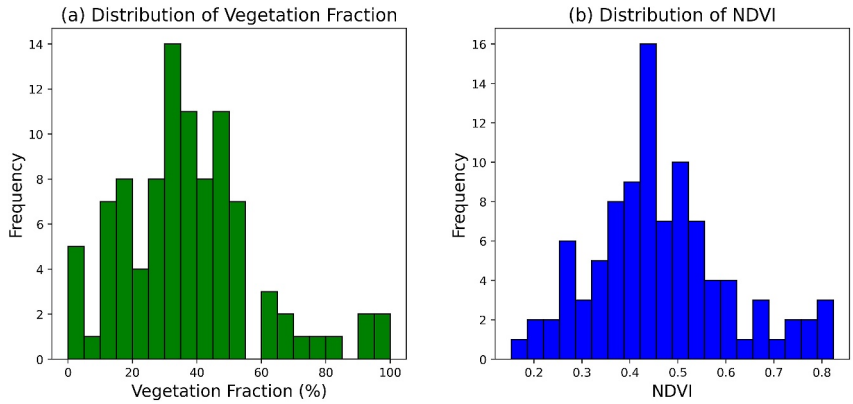


**Figure 3.** Histograms illustrating (a) the distribution of vegetation fraction (%) and (b) NDVI values derived from hyperspectral imaging data at ground truth locations. The histograms depict the frequency distribution of vegetation coverage and NDVI values across our study area, indicating a moderately to highly dense vegetated area.

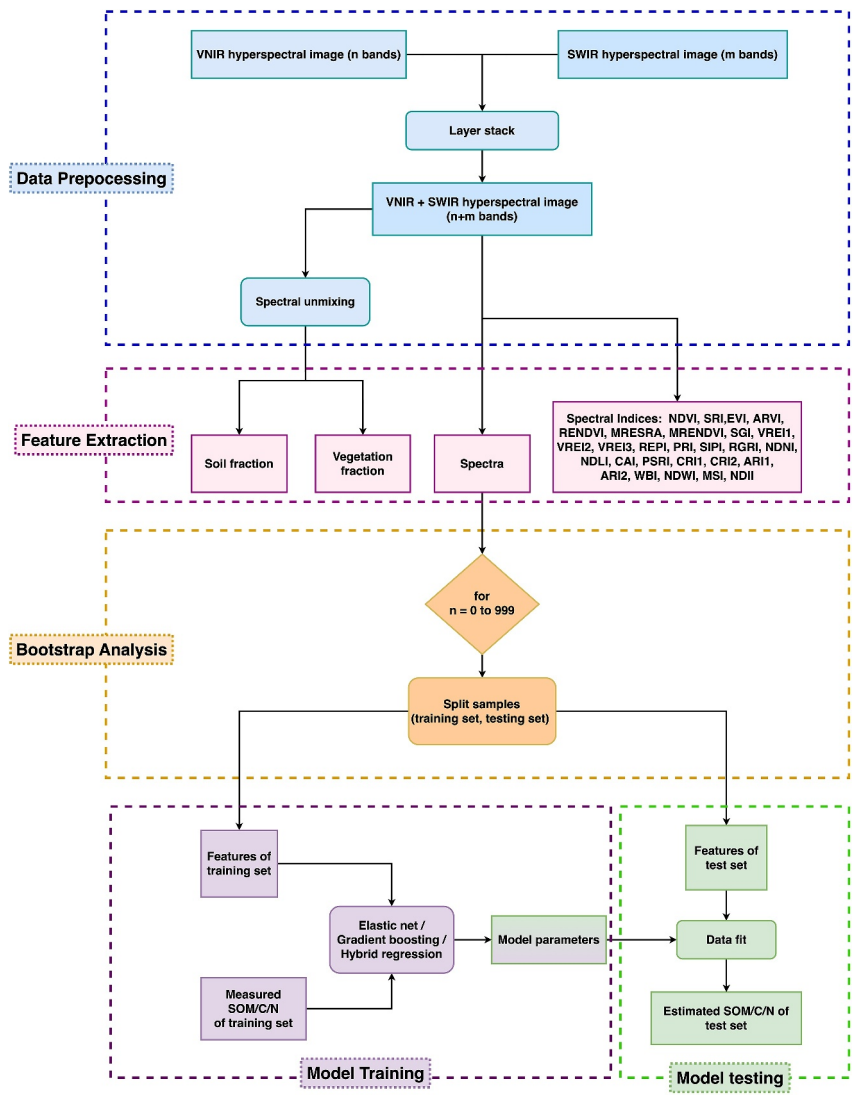


**Figure 4.** Flowchart illustrating the workflow of this study, outlining the sequential steps and processes involved in our research methodology.

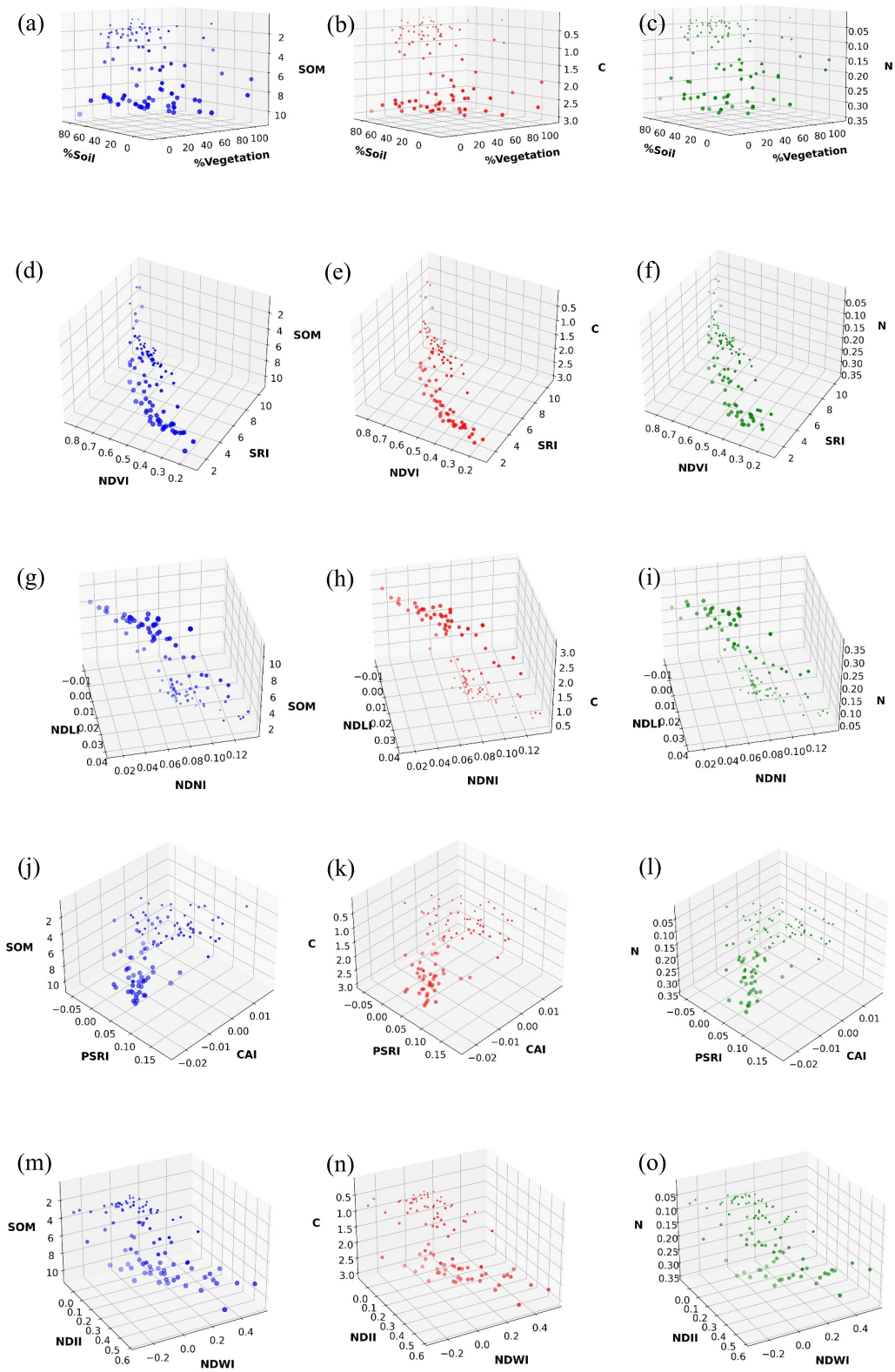


**Figure 5.** 3D scatter plots between selected input features and soil properties: (left column) soil organic matter (SOM), (middle column) total carbon (C), and (right column) total nitrogen (N). The plots depict these soil properties versus (a–c) soil and vegetation fractions. (d–f) NDVI and SRI. (g–i) NDLI and NDNI. (j–l) PSRI and CAI. (m–o) NDII and NDWI, with each series showing relationships with SOM, C, and N, respectively. The size of the points increases with the magnitude of the target soil component (SOM, C, or N), providing a visual representation of higher values.

#### 3.2.3. Hybrid Model: Stacked ENet and GBRT

Finally, we employed a stacked generalization approach (Wolpert, 1992) to integrate the predictions from ENet and GBRT to enhance prediction accuracy. Stacking is an ensemble learning technique that involves training multiple base models and combining their outputs using a meta-model. The base models—ENet and GBRT—were first trained on the training data set in our implementation. ENet was chosen for its ability to handle multicollinearity and perform feature selection using L1 norm (lasso) and L2 norm (ridge) regularization, while GBRT was selected for its capacity to model complex, nonlinear relationships through iterative learning. The outputs (predictions) from these base models were then used as new features for the meta-model, which, in our case, is a linear regression model. This meta-model learns to optimally combine the base model predictions by minimizing prediction error on a validation data set. This approach leverages the strengths of both base models—ENet's feature selection capabilities and GBRT's nonlinear modeling power—leading to improved predictive performance and robustness. Combining the predictions from ENet and GBRT, the stacked model can capture a broader range of relationships within the data, resulting in a more accurate and generalizable model. This stacked ensemble is particularly effective in dealing with high-dimensional data sets with complex interactions between variables.

### 3.3. Evaluation of Model Performance

We evaluate the accuracy of our models using the normalized root mean square errors (NRMSE) and the coefficient of determination ($R^2$) metrics. These metrics are crucial for assessing model performance and ensuring precise SOM, C, and N predictions. NRMSE, also known as the "Scatter Index", is defined as (Bonakdar et al., 2016; Kisi et al., 2013) follows:

$$NRMSE = \frac{\sqrt{\frac{1}{M}\sum_{k=1}^{M}\left(Y_{k,\text{predicted}} - Y_{k,\text{measured}}\right)^2}}{\overline{Y_{\text{measured}}}}, \tag{2}$$

and $R^2$ is given by

$$R^2 = 1 - \frac{\sum_{k=1}^{M}\left(Y_{k,\text{predicted}} - Y_{k,\text{measured}}\right)^2}{\sum_{k=1}^{M}\left(Y_{k,\text{measured}} - \overline{Y_{\text{measured}}}\right)^2}. \tag{3}$$

In these equations, $Y_{k,\text{predicted}}$ and $Y_{k,\text{measured}}$ denote the predicted and observed values for SOM, C, and N of the $k$th instance, respectively, with $M$ representing the total number of observations and $\overline{Y_{\text{measured}}}$ the mean observed value across the data set. The scatter index normalizes prediction errors, allowing for fair comparisons across different data sets or units, while $R^2$ highlights the proportion of variance in SOM, C, and N explained by the model, illustrating its explanatory power and predictive accuracy.

We conducted a comprehensive bootstrap analysis with 1,000 iterations to evaluate the proposed models, ensuring the robustness and reliability of the predictive models. At each iteration of the bootstrap analysis, we randomly split the samples into a training set (80%) and a test set (20%), allowing us to train the model on one subset of the data and evaluate its performance on an independent subset. This extensive resampling approach allows us to assess the stability of our predictions and understand the variability of the NRMSE and $R^2$ metrics under different sample conditions. The choice of 1,000 iterations strikes a balance between computational efficiency and the statistical robustness of the results, providing a comprehensive view of the model's performance across a wide range of potential scenarios. This iterative training and testing process helps minimize bias in the model's predictions, ensuring that the evaluation metrics reflect the model's true predictive capability.

## 4. Results

Table 2 presents the performance evaluation of the three predictive models— ENet, GBRT, and the hybrid model combining both techniques—in predicting SOM, C, and N through a 1,000-iteration bootstrap analysis. The hybrid model consistently outperformed the other models in estimating SOM, achieving a lower mean NRMSE of 0.118 than 0.133 for ENet and 0.134 for GBRT. It also recorded a reduced median NRMSE of 0.112. All three models had a notably tight standard deviation of the NRMSE in the range 0.040–0.042, indicating low variability

**Table 2**
*Model Evaluation on Test Sets From 1,000-Iteration Bootstrap Analysis*

| | | Models | | |
|---|---|---|---|---|
| SOM/C/N | Evaluation metrics | Elastic net (ENet) regression | Gradient-boosted regression trees (GBRT) | Hybrid model: stacked ENet and GBRT |
| Soil organic matter (SOM) | Mean NRMSE | 0.133 | 0.134 | 0.118 |
| | Median NRMSE | 0.127 | 0.130 | 0.112 |
| | Minimum NRMSE | 0.052 | 0.036 | 0.029 |
| | Standard deviation of NRMSE | 0.041 | 0.040 | 0.042 |
| | Mean $R^2$ value | 0.842 | 0.841 | 0.874 |
| | Median $R^2$ value | 0.874 | 0.868 | 0.901 |
| | Maximum $R^2$ value | 0.978 | 0.988 | 0.993 |
| | Standard deviation of $R^2$ value | 0.112 | 0.102 | 0.097 |
| Total carbon (C) | Mean NRMSE | 0.141 | 0.143 | 0.127 |
| | Median NRMSE | 0.131 | 0.138 | 0.118 |
| | Minimum NRMSE | 0.042 | 0.008 | 0.029 |
| | Standard deviation of NRMSE | 0.053 | 0.048 | 0.045 |
| | Mean $R^2$ value | 0.827 | 0.829 | 0.865 |
| | Median $R^2$ value | 0.871 | 0.860 | 0.896 |
| | Maximum $R^2$ value | 0.988 | 0.999 | 0.995 |
| | Standard deviation of $R^2$ value | 0.172 | 0.119 | 0.101 |
| Total nitrogen (N) | Mean NRMSE | 0.168 | 0.141 | 0.138 |
| | Median NRMSE | 0.160 | 0.141 | 0.135 |
| | Minimum NRMSE | 0.084 | 0.042 | 0.041 |
| | Standard deviation of NRMSE | 0.047 | 0.038 | 0.038 |
| | Mean $R^2$ value | 0.737 | 0.815 | 0.822 |
| | Median $R^2$ value | 0.780 | 0.831 | 0.845 |
| | Maximum $R^2$ value | 0.947 | 0.986 | 0.986 |
| | Standard deviation of $R^2$ value | 0.188 | 0.102 | 0.100 |

and high consistency of predictions across bootstrap iterations for comparison. In predicting C, the hybrid model reported the lowest mean NRMSE at 0.127 and the lowest median NRMSE at 0.118, underscoring its superior accuracy. The standard deviation for the hybrid model was the smallest at 0.045, illustrating consistent performance across different bootstrap samples. Compared with ENet and GBRT, which showed higher NRMSE values, the hybrid model's robustness was evident, particularly in handling data set complexities and variabilities. For N, ENet recorded the highest mean NRMSE of 0.168, while the GBRT model had a mean NRMSE of 0.141, and the hybrid model achieved slightly better performance with a mean NRMSE of 0.138. Similarly, the hybrid model performed marginally better with a slightly lower median NRMSE of 0.135 than GBRT's 0.141 and obtained a lower standard deviation of 0.038, the same obtained with GBRT, than the result obtained by ENet, 0.047. Overall, the hybrid model produced the best results.

The $R^2$ values reinforce these results, with the hybrid model achieving consistently higher mean and median $R^2$ values across all parameters. It reached a mean $R^2$ of 0.874 for SOM, surpassing both ENet (0.842) and GBRT (0.841). For carbon, the hybrid model recorded a mean $R^2$ of 0.865, higher than ENet (0.827) and GBRT (0.829). The hybrid model for N also outperformed the other models with a mean $R^2$ of 0.822, ahead of ENet (0.737) and GBRT (0.815). The lower standard deviation of $R^2$ values for the hybrid model across all predictions emphasizes its accuracy and consistency in diverse data splits. Histograms detailing the bootstrap outcomes for NRMSE and $R^2$ (shown in Figures 6–8) visually illustrate these metrics across predictions for SOM, C, and N and showcase the

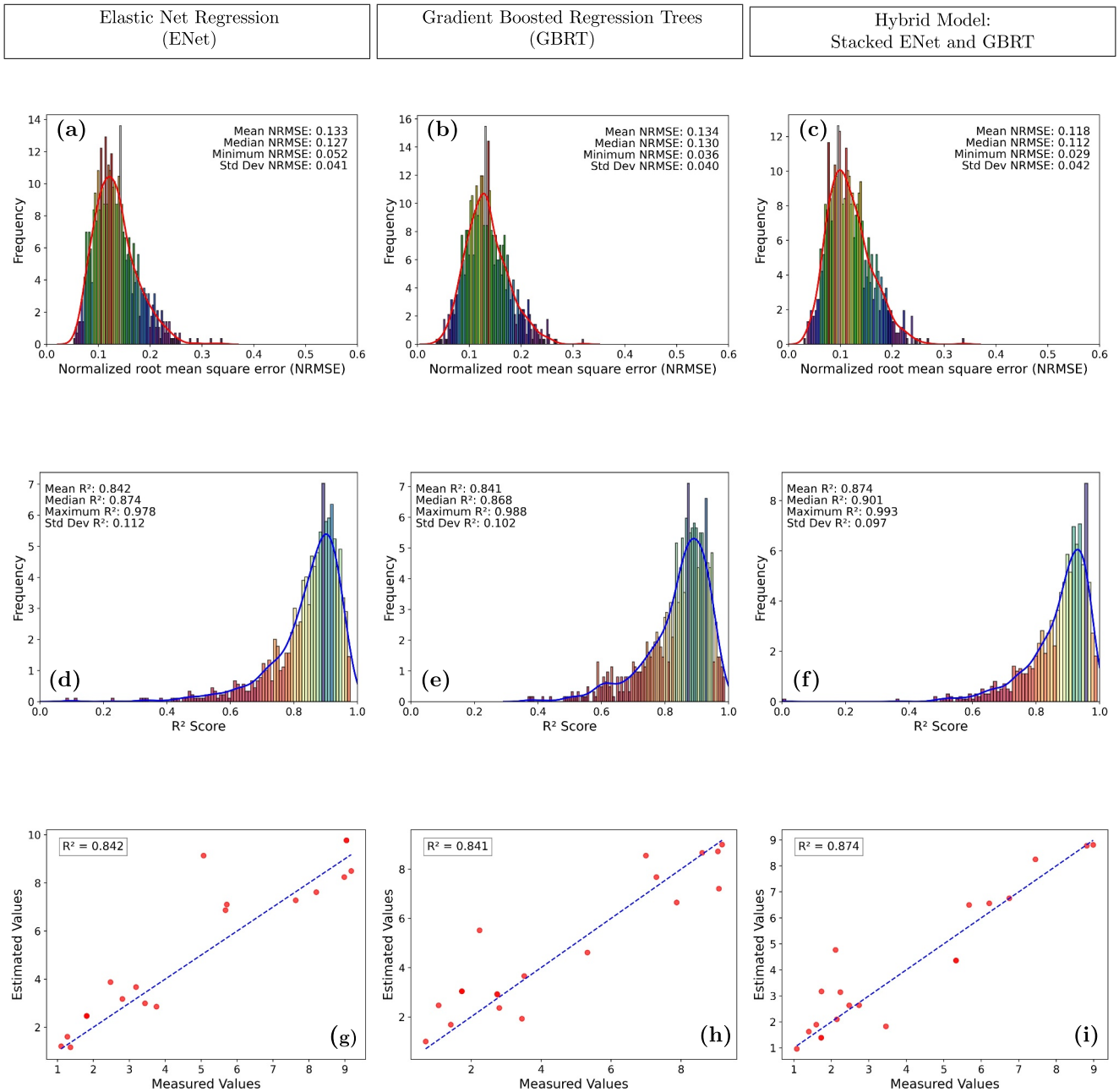


**Figure 6.** Bootstrap analysis of the soil organic matter retrieval model over 1,000 iterations, evaluated using test data. The figure displays histograms for normalized root mean square error (row 1) and $R^2$ (row 2) values, along with near-mean estimated versus measured plots (row 3). Columns represent different models: (a), (d), and (g) elastic net regression; (b), (e), and (h) gradient-boosted regression trees; and (c), (f), and (i) a hybrid model combining elastic net and gradient-boosted regression trees.

hybrid model's narrower spread and higher peaks, indicating its robustness and effectiveness in handling complex and varied ecological data sets.

Figure 9 presents the feature importance plots, emphasizing how the hybrid model synthesizes various indicators to enhance prediction accuracy. This capability allows it to capture both linear and nonlinear relationships effectively, optimizing its performance. The top-performing instances depicted in Figure 10 highlight that optimal performance can consistently be achieved with sufficient training data. Figure 11 shows the predicted spatial distribution of SOM, C, and N across a selected transect of the study site, derived from the hybrid model. On each map, areas with higher vegetation fractions show higher SOM, C, and N values. This pattern is consistent with

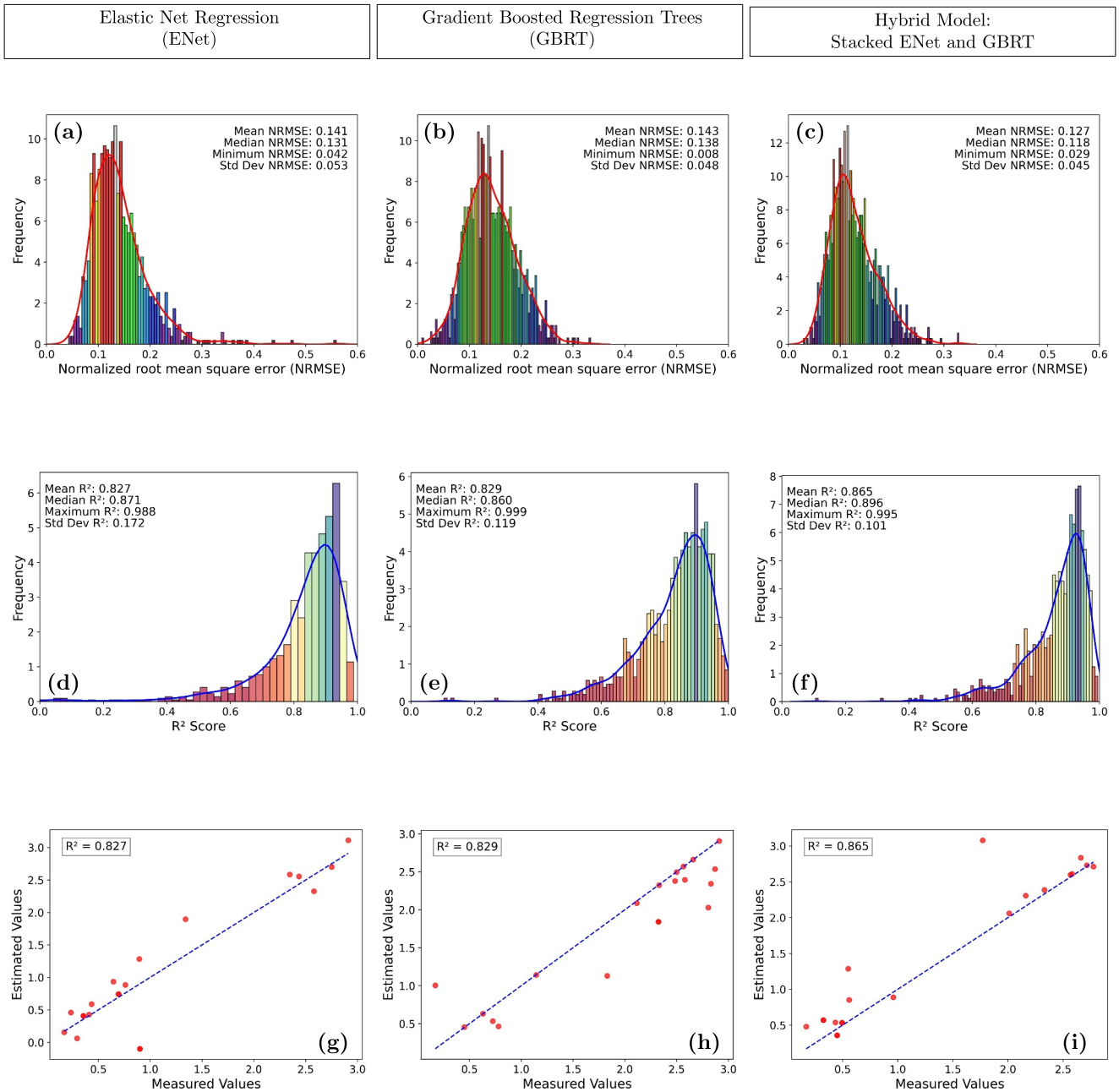


**Figure 7.** Bootstrap analysis of the soil total carbon retrieval model over 1,000 iterations, evaluated using test data. The figure displays histograms for normalized root mean square error (row 1) and $R^2$ (row 2) values, along with near-mean estimated versus measured plots (row 3). Columns represent different models: (a), (d), and (g) elastic net regression; (b), (e), and (h) gradient-boosted regression trees; and (c), (f), and (i) a hybrid model combining elastic net and gradient-boosted regression trees.

commonly observed relationships in salt marshes, where vegetated areas, especially those dominated by *Spartina alterniflora* tend to receive higher organic inputs from both above-ground and below-ground biomass, leading to higher SOM and nutrient concentrations. Sparsely vegetated sites show lower SOM, C, and N values due to a smaller input of organic matter. The model's reliance on vegetation and surface features helps explain this spatial pattern. Figure 9 shows that ENet tended to emphasize individual reflectance bands in the shortwave infrared and surface features such as vegetation-soil fractions while identifying a range of vegetation-sensitive indices as moderately important. In contrast, GBRT prioritized nonlinear combinations of vegetation and moisture-sensitive indices such as NDNI, NDLI, CAI, PSRI, NDWI, and WBI, along with vegetation-soil fractions. Among these,

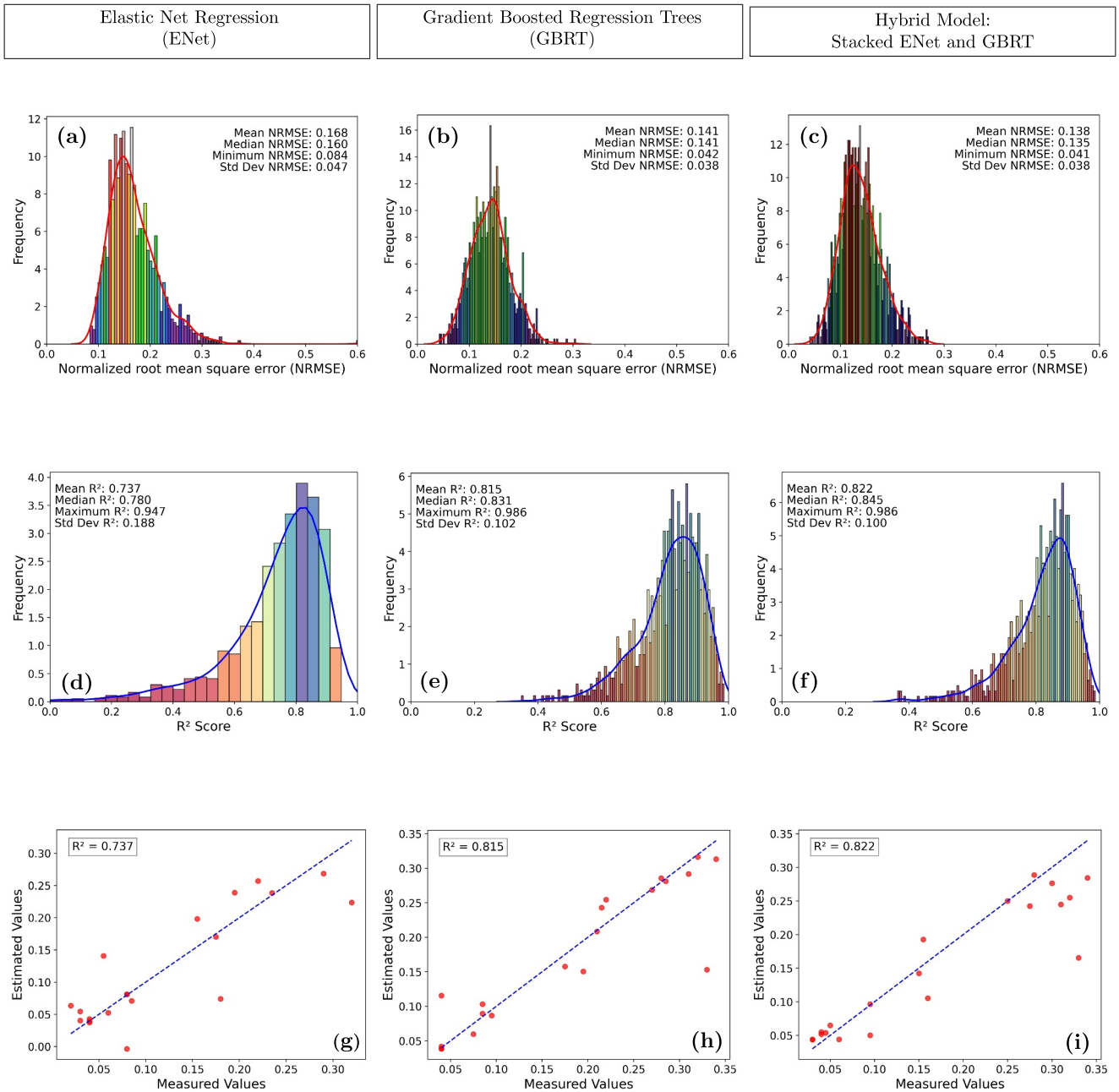


**Figure 8.** Bootstrap analysis of the soil total nitrogen retrieval model over 1,000 iterations, evaluated using test data. The figure displays histograms for normalized root mean square error (row 1) and $R^2$ (row 2) values, along with near-mean estimated versus measured plots (row 3). Columns represent different models: (a), (d), and (g) elastic net regression; (b), (e), and (h) gradient-boosted regression trees; and (c), (f), (i) a hybrid model combining elastic net and gradient-boosted regression trees.

NDNI was the most influential in the GBRT model and represented more than 20% of importance in features. The hybrid model leveraged both strategies to effectively capture spatial variability in soil properties.

## 5. Discussion

The results of this study demonstrate the benefit of combining SIs, reflectance values, and soil-vegetation fraction estimates for the improved prediction of SOM, C, and N in salt marsh environments. The model incorporates vegetation structure and soil properties by including a range of spectral features, leading to enhanced predictions. SOM, C, and N spatial distribution patterns reflect the value of incorporating more than one spectral predictor

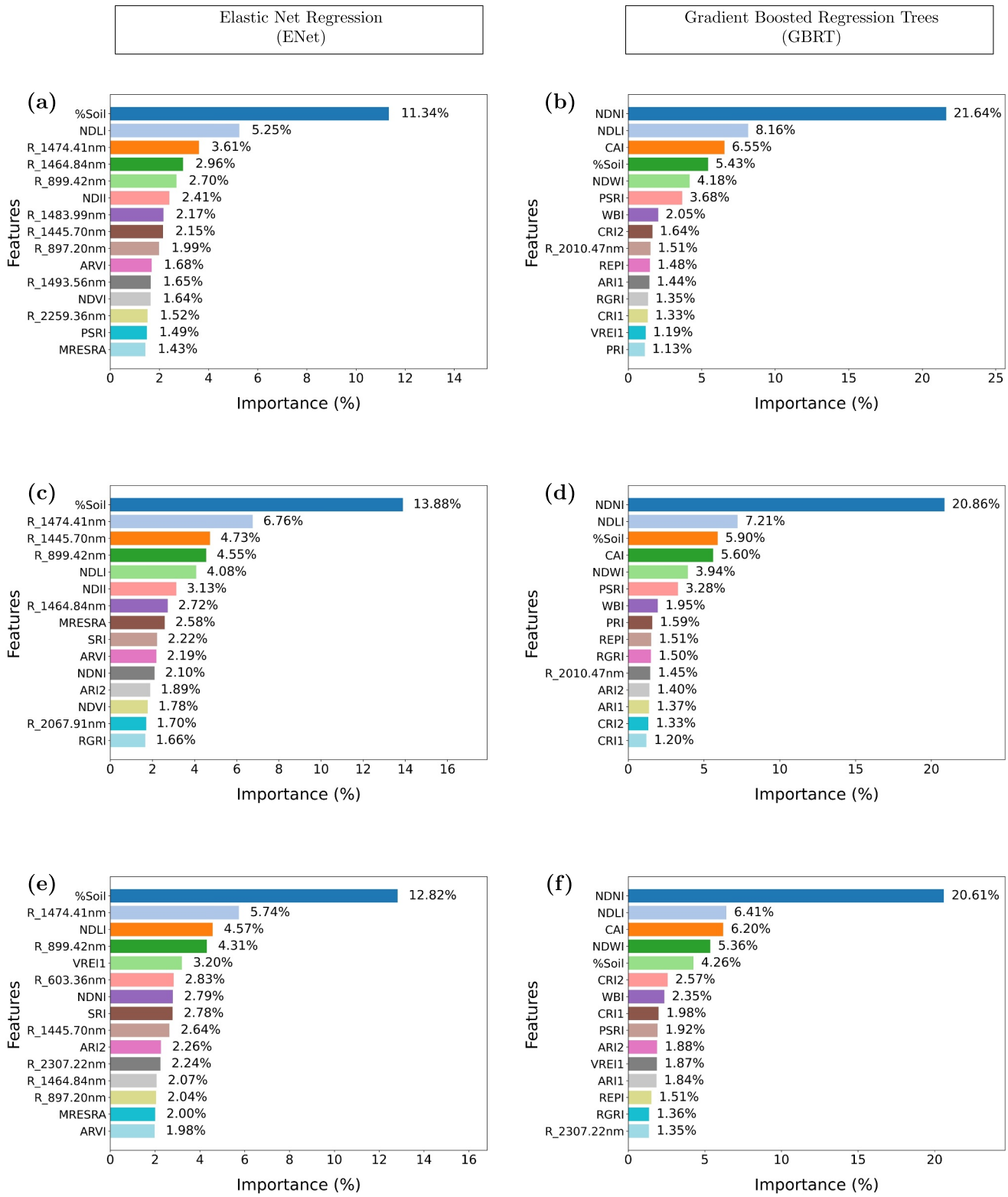


**Figure 9.** Importance of the top 15 features for each model, expressed as percentages. Rows 1–3 represent the retrieval of soil organic matter, total carbon, and total nitrogen, respectively. Columns 1–2 distinguish between the elastic net regression and gradient-boosted regression trees models, respectively.

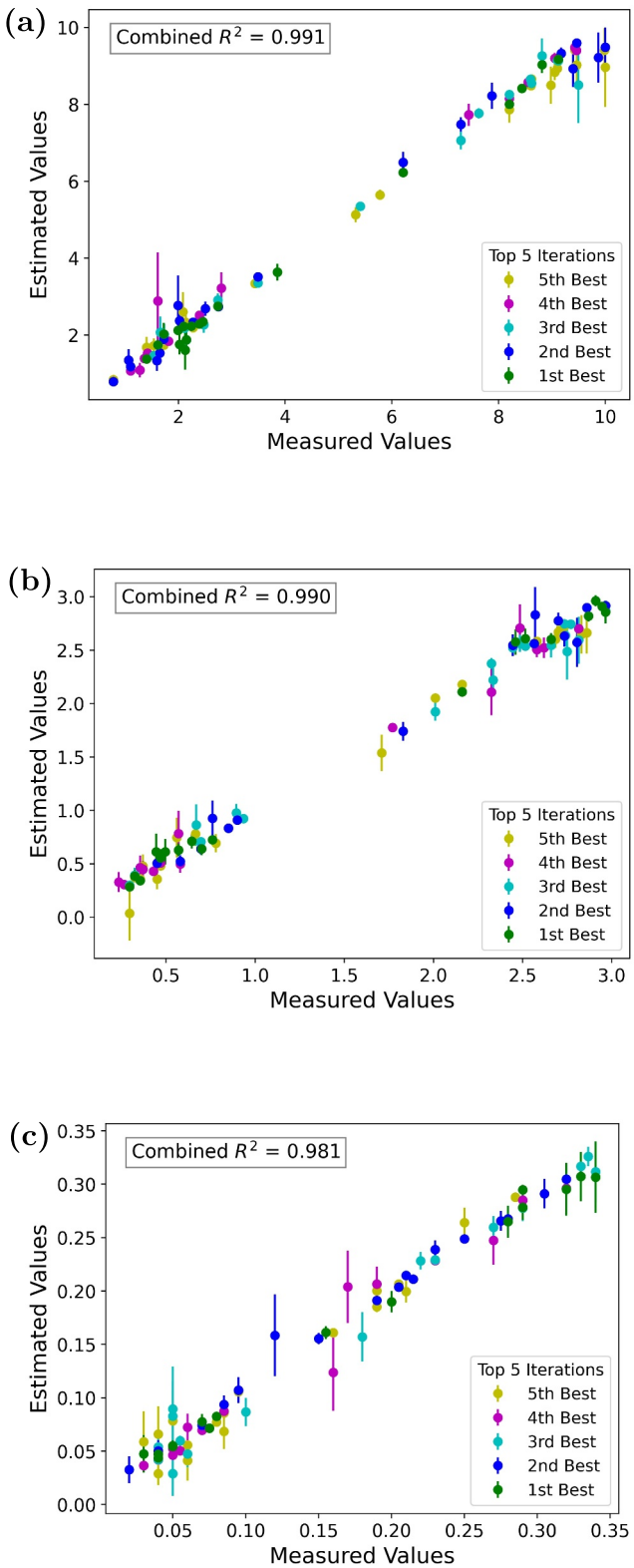


**Figure 10.**

because both biotic and abiotic processes control salt marsh soil characteristics. Feature importance analysis from Figure 9 indicates that NDVI, PSRI, NDWI, NDLI, NDNI, CAI, and WBI are among the most significant SIs for retrieving SOM, C, and N. These indices consistently contribute to model performance across all three parameters, demonstrating their relevance in characterizing vegetation and soil properties. NDVI and PSRI are vegetation indices that provide information about plant senescence and health, which directly relate to decomposition and organic matter buildup. NDNI, a vegetation index, measures canopy nitrogen concentration and is used to estimate soil nitrogen availability. NDLI, which measures lignin content in vegetation, is also important in understanding organic matter input to soils, as lignin-rich plant material decomposes at different rates and influences soil composition. On the other hand, CAI, NDWI, and WBI provide insights into both vegetation and soil properties. CAI provides information on organic matter composition because cellulose is a dominant organic matter component of decomposing plant residues that contribute to SOM. NDWI is primarily used to estimate vegetation water content but can also serve as an indirect indicator of soil moisture in sparsely vegetated or bare soil areas, a critical factor for the decomposition and stabilization of organic matter. WBI is related to both vegetation and soil water content (Curcio & Petty, 1951), providing the overall model with an input that can help explain and assess hydrological variability impacting SOM, C, and N. In addition to SIs, several individual reflectance bands were identified as top predictors in feature importance analysis for both ENet and GBRT. Many of these bands correspond to known water absorption features, particularly near 1,400 nm and 1,900–2,000 nm, which are sensitive to soil moisture variations and influenced by soil porosity. As soil moisture affects decomposition of organic matter and nutrient holding capacity, these bands can offer indirect information about carbon and nitrogen storage. By incorporating both reflectance values and SIs, the model can effectively capture vegetation and soil's structural and biochemical properties. Model performance with different input feature sets is shown in Table 3. The output indicates that a combination of SIs, reflectance, and soil-vegetation fraction gives the best SOM, C, and N predictions, leading to more robust and reliable predictions across varying salt marsh conditions.

Including soil-vegetation fraction improves model precision by enabling the discrimination between soil and vegetation contributions in every pixel. The fraction gives the model useful contextual information because spectral responses differ significantly from dense vegetation to bare soil. As vegetation and soil cover differ, vegetation-related spectral index values and soil reflectance features change correspondingly to reflect the changing contributions of each factor. This variation allows the model to cope better with these changing conditions and improve the estimation of SOM, C, and N across diverse mixtures of soil and vegetation in the salt marsh landscape. Ground truth data used in this study were acquired from a range of sites, from bare soil patches to densely vegetated patches, so the model was trained on a diversity of salt marsh conditions. The SOM, C, and N patterns resemble well-documented ecological processes in salt marshes. High SOM and C

**Figure 10.** Estimated versus measured values for test samples in the top five cases out of 1,000 iterations using the hybrid model (stacked elastic net regression and gradient-boosted regression trees). (a–c) represent soil organic matter, total carbon, and total nitrogen retrieval models, respectively. The error bars represent absolute residuals, indicating the deviation of predictions from measured values.

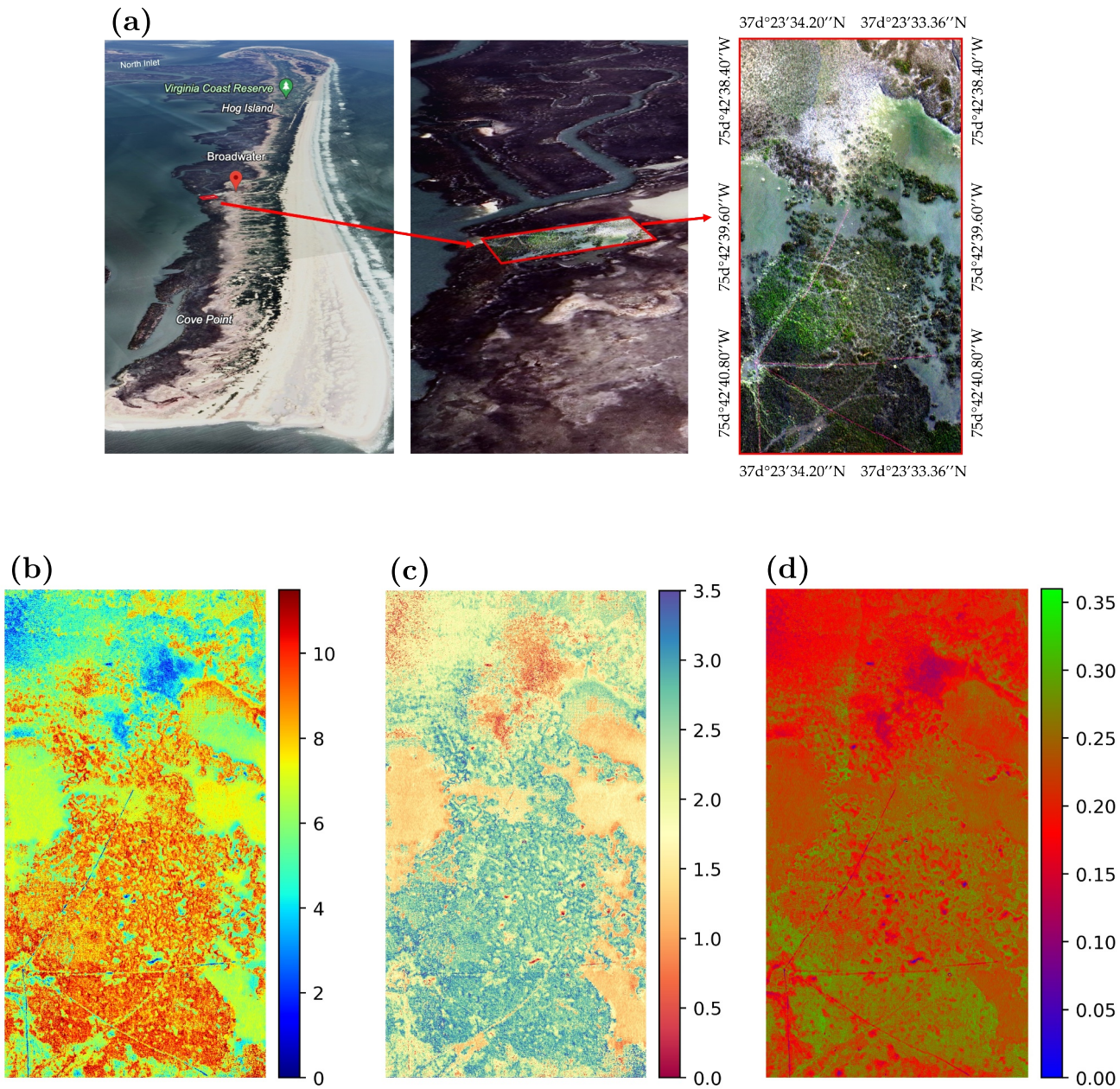


**Figure 11.** Mapping of (a) RGB bands from one of the hyperspectral scenes (right) superimposed on a Google Earth image (left and middle) to show the location and predicted (b) percent soil organic matter, (c) percent total carbon, and (d) percent total nitrogen derived from unmanned aerial systems hyperspectral images taken on 27 July 2019 over a region of salt marshes on Hog Island at the Virginia Coast Reserve LTER.

levels coincide with older marsh areas where there has been time for organic matter to accumulate and low levels in younger marshes where sedimentation has been more recent. The spatial distribution of SOM, C, and N in Figure 11 primarily represents mature marsh regions and their surrounding areas, where prolonged biomass deposition and microbial decomposition have contributed to higher SOM and nutrient accumulation. Given the proximity to mature marsh environments, high SOM, C, and N values were expected, and the model's predictions align with these ecological patterns. An interaction among vegetation cover, organic inputs, and local hydrology likely controls spatial distributions in Figure 11. More densely vegetated areas with *Spartina alterniflora* have higher SOM, C, and N concentrations, likely due to greater organic inputs from litter and root turnover. Furthermore, plant-soil interactions in these zones may alter soil oxygen dynamics, influencing decomposition and nutrient cycling near the root zone. While not modeled explicitly, subtle changes in microtopography can

**Table 3**
*Comparison of Hybrid Model Performance on Test Sets From a 1,000-Iteration Bootstrap Analysis for Predicting SOM, C, and N Using Different Input Features*

| | | Model inputs | | |
|---|---|---|---|---|
| Prediction target | Evaluation metric | Reflectance | Spectral indices + soil/veg fraction | Reflectance + spectral indices + soil/veg fraction |
| Soil organic matter (SOM) | Mean NRMSE | 0.127 | 0.148 | 0.118 |
| | Mean $R^2$ | 0.863 | 0.807 | 0.874 |
| Total carbon (C) | Mean NRMSE | 0.132 | 0.143 | 0.127 |
| | Mean $R^2$ | 0.860 | 0.825 | 0.865 |
| Total nitrogen (N) | Mean NRMSE | 0.159 | 0.152 | 0.138 |
| | Mean $R^2$ | 0.775 | 0.787 | 0.822 |

affect inundation frequency, sediment deposition, and the distribution of plants, all of which impact soil carbon and nitrogen processes. The model could capture parallel spatial patterns in all three because of the strong ecosystem feedback processes that ultimately control SOM, C, and N. Figure S1 further confirms that SOM, C, and N exhibit a strong linear relationship, indicating that similar biochemical and environmental factors influence these variables. The close correlation among these variables attests that one modeling strategy is sufficient for predicting all three parameters. Because SOM is a significant carbon and nitrogen source in marsh soils, the SIs associated with SOM—especially those related to vegetation structure, biomass, and organic content—also offer good predictive capacity for C and N. The fact that the same model structure works for all three variables is a measure of its robustness, and it argues for the use of the identical set of spectral features for SOM, C, and N estimation.

Although the model worked satisfactorily, additional improvements would render it more transferable to other wetland environments. Extension of the data set to cover samples from various sites with varying environmental conditions would render the model more general. Furthermore, including physically based modeling methods that account for soil and vegetation optical properties would render it more transferable. Future research should also cover the impact of changing vegetation and soil properties throughout the seasons on model performance because multiseason data sets better optimize the prediction and stabilize the model. Expansion of these approaches to larger spatial scales represents another important research direction. Though UAS-based hyperspectral imaging provides high-resolution measurements, modifying this approach to satellite-borne hyperspectral sensors would facilitate monitoring at the regional or the global scale. Synthesis of hyperspectral data from current and future satellite missions would allow long-term wetland monitoring, enhance carbon and nitrogen budgeting, and facilitate conservation activities. Combining airborne and satellite hyperspectral data with robust statistical modeling would bridge the gap between intensive field-based sampling and the extensive use of remote sensing for soil property prediction. The findings of this research illustrate how the utilization of multiple sources of spectrally dependent inputs—integrating SIs, reflectance values, and soil-vegetation fraction estimates—enhances the precision of soil property prediction in salt marshes. The model can successfully represent the complex interactions that control SOM, C, and N distributions by integrating vegetation and soil spectral characteristics. Future efforts are needed to advance model transferability with physically based modeling, expand training data sets for greater robustness, and scale up these approaches to large-scale satellite applications. These actions will improve coastal wetland monitoring and management, especially under changing climate and related wetland land-cover change that impacts carbon sequestration.

## 6. Conclusion

We harnessed the capabilities of UAS-based hyperspectral imagery to develop and validate models for estimating fundamental soil properties—SOM, C, and N—in the complex and variably vegetated salt marshes of Hog Island, VA. Utilizing UAS technology enabled the acquisition of high-resolution spectral data across the VNIR and SWIR spectral ranges at high spatial resolution, crucial for capturing the detailed spatial variability of soil properties. This approach allowed us to utilize a range of SIs and reflectance data as features in our models. These features were specifically chosen for their proven sensitivity to variations in soil properties and vegetation health, making them highly relevant to our study's objectives. By combining ENet and GBRT into a hybrid model, we

substantially enhanced the accuracy of our predictions for these key soil metrics. By integrating the strengths of ENet and GBRT together, we were able to consistently outperform the individual models, reducing NRMSE and improving $R^2$ values, affirming the hybrid model's effectiveness in capturing both linear and nonlinear relationships inherent in ecological data. This performance highlights the value of blending different modeling techniques to tackle the complex interdependencies observed in environmental data sets.

This study illustrates the potential of combining advanced statistical modeling methods and high-resolution remote sensing data to improve soil property estimation in ecologically sensitive areas. Our results offer a robust framework for ecological monitoring and management. The approach used here, when applied across a range of salt marsh environments, has excellent potential to contribute to our knowledge of soil properties, enabling remote assessment of carbon sequestration, nutrient status, and potential for climate mitigation. Future research will focus on refining these models and extending their application to other environmental contexts, broadening their impact on sustainable ecosystem management.

## Data Availability Statement

The relevant data set and code are publicly available on Zenodo: DOI: https://doi.org/10.5281/zenodo.14994443 (Nur, 2025). For the most recent updates, please visit the GitHub repository: https://github.com/grit-lab/grit-lab-soil-carbon-nitrogen-organic-matter-public-facing-repo.

**Acknowledgments**
Our 2019 field campaign that provided data for the study described here was supported in part by the National Science Foundation's Division of Environmental Biology (NSF DEB) Grants 1237733 and 1832221 to the Virginia Coast Reserve Long-Term Ecological Research (VCR-LTER) site, as well as by an Explorer Grant from the National Geographic Society (Grant NGS-382R-18). Additionally, we appreciate the assistance of Sydney VanWinkle and Sarah Ponte Cabral during the field campaign.

## References

Aryal, D. R., De Jong, B. H., Ochoa-Gaona, S., Esparza-Olguin, L., & Mendoza-Vega, J. (2014). Carbon stocks and changes in tropical secondary forests of southern Mexico. *Agriculture, Ecosystems & Environment*, *195*, 220–230. https://doi.org/10.1016/j.agee.2014.06.005

Aryal, D. R., De Jong, B. H., Ochoa-Gaona, S., Mendoza-Vega, J., & Esparza-Olguin, L. (2015). Successional and seasonal variation in litterfall and associated nutrient transfer in semi-evergreen tropical forests of se Mexico. *Nutrient Cycling in Agroecosystems*, *103*(1), 45–60. https://doi.org/10.1007/s10705-015-9719-0

Aryal, D. R., Morales Ruiz, D. E., Tondopo Marroquin, C. N., Pinto Ruiz, R., Guevara Hernandez, F., Venegas Venegas, J. A., et al. (2018). Soil organic carbon depletion from forests to grasslands conversion in Mexico: A review. *Agriculture*, *8*(11), 181. https://doi.org/10.3390/agriculture8110181

Ashman, M., & Puri, G. (2013). *Essential soil science: A clear and concise introduction to soil science*. John Wiley and Sons.

Bachmann, C., Nur, N., Lapszynski, C., Shiltz, D., Golding, R., & Lee, C. (2021). Retrieval of sediment geophysical properties from hyperspectral UAS imagery in preparation for the NASA SBG mission. *AGU fall meeting abstracts*, *2021*. GC11A–05.

Bachmann, C. M., Bettenhausen, M. H., Fusina, R. A., Donato, T. F., Russ, A. L., Burke, J. W., et al. (2003). A credit assignment approach to fusing classifiers of multiseason hyperspectral imagery. *IEEE Transactions on Geoscience and Remote Sensing*, *41*(11), 2488–2499. https://doi.org/10.1109/tgrs.2003.818537

Bachmann, C. M., Donato, T. F., Lamela, G. M., Rhea, W. J., Bettenhausen, M. H., Fusina, R. A., et al. (2002). Automatic classification of land cover on Smith Island, VA, using HyMAP imagery. *IEEE Transactions on Geoscience and Remote Sensing*, *40*(10), 2313–2330. https://doi.org/10.1109/tgrs.2002.804834

Bangelesa, F., Adam, E., Knight, J., Dhau, I., Ramudzuli, M., & Mokotjomela, T. M. (2020). Predicting soil organic carbon content using hyperspectral remote sensing in a degraded mountain landscape in Lesotho. *Applied and environmental soil science*, *2020*, 1–11. https://doi.org/10.1155/2020/2158573

Bao, Y., Ustin, S., Meng, X., Zhang, X., Guan, H., Qi, B., & Liu, H. (2021). A regional-scale hyperspectral prediction model of soil organic carbon considering geomorphic features. *Geoderma (Amsterdam)*, *403*, 115263. https://doi.org/10.1016/j.geoderma.2021.115263

Birth, G. S., & McVey, G. R. (1968). Measuring the color of growing turf with a reflectance spectrophotometer[1]. *Agronomy Journal*, *60*(6), 640–643. https://doi.org/10.2134/agronj1968.00021962006000060016x

Bonakdar, L., Oumeraci, H., & Etemad-Shahidi, A. (2016). Run-up on vertical piles due to regular waves: Small-scale model tests and prediction formulae. *Coastal Engineering*, *118*, 1–11. https://doi.org/10.1016/j.coastaleng.2016.08.008

Bortolus, A., Adam, P., Adams, J. B., Ainouche, M. L., Ayres, D., Bertness, M. D., et al. (2019). Supporting Spartina: Interdisciplinary perspective shows Spartina as a distinct solid genus. *Ecology*, *100*(11). https://doi.org/10.1002/ecy.2863

Castaldi, F., Palombo, A., Santini, F., Pascucci, S., Pignatti, S., & Casa, R. (2016). Evaluation of the potential of the current and forthcoming multispectral and hyperspectral imagers to estimate soil texture and organic carbon. *Remote Sensing of Environment*, *179*, 54–65. https://doi.org/10.1016/j.rse.2016.03.025

Ceccato, P., Flasse, S., Tarantola, S., Jacquemoud, S., & Grégoire, J.-M. (2001). Detecting vegetation leaf water content using reflectance in the optical domain. *Remote Sensing of Environment*, *77*(1), 22–33. https://doi.org/10.1016/s0034-4257(01)00191-2

Chahl, J. (2015). Unmanned aerial systems (UAS) research opportunities. *Aerospace*, *2*(2), 189–202. https://doi.org/10.3390/aerospace2020189

Chaity, M. D., & van Aardt, J. (2024). Exploring the limits of species identification via a convolutional neural network in a complex forest scene through simulated imaging spectroscopy. *Remote Sensing*, *16*(3), 498. https://doi.org/10.3390/rs16030498

Champagne, C., PATTEY, E., BANNARI, A., & S, I. B. (2001). Mapping crop water stress: Issues of scale in the detection of plant water status using hyperspectral indices. In *Mesures physiques et signatures en télédétection (aussois, 8-12 january 2001)* (pp. 79–84).

Curcio, J. A., & Petty, C. C. (1951). The near infrared absorption spectrum of liquid water. *Journal of the Optical Society of America*, *41*(5), 302–304. https://doi.org/10.1364/josa.41.000302

Curran, P. J., Windham, W. R., & Gholz, H. L. (1995). Exploring the relationship between reflectance red edge and chlorophyll concentration in slash pine leaves. *Tree Physiology*, *15*(3), 203–206. https://doi.org/10.1093/treephys/15.3.203

Datt, B. (1999). A new reflectance index for remote sensing of chlorophyll content in higher plants: Tests using eucalyptus leaves. *Journal of Plant Physiology*, *154*(1), 30–36. https://doi.org/10.1016/s0176-1617(99)80314-9

Datta, D., Paul, M., Murshed, M., Teng, S. W., & Schmidtke, L. (2022). Soil moisture, organic carbon, and nitrogen content prediction with hyperspectral data using regression models. *Sensors*, *22*(20), 7998. https://doi.org/10.3390/s22207998

Daughtry, C., Hunt Jr, E., & McMurtrey Iii, J. (2004). Assessing crop residue cover using shortwave infrared reflectance. *Remote Sensing of Environment*, *90*(1), 126–134. https://doi.org/10.1016/j.rse.2003.10.023

Daughtry, C. S. (2001). Discriminating crop residues from soil by shortwave infrared reflectance. *Agronomy Journal*, *93*(1), 125–131. https://doi.org/10.2134/agronj2001.931125x

Deegan, L. A., Johnson, D. S., Warren, R. S., Peterson, B. J., Fleeger, J. W., Fagherazzi, S., & Wollheim, W. M. (2012). Coastal eutrophication as a driver of salt marsh loss. *Nature*, *490*(7420), 388–392. https://doi.org/10.1038/nature11533

De Mol, C., De Vito, E., & Rosasco, L. (2009). Elastic-net regularization in learning theory. *Journal of Complexity*, *25*(2), 201–230. https://doi.org/10.1016/j.jco.2009.01.002

Envi (2024a). Atmospheric correction via empirical line method. Retrieved from https://www.nv5geospatialsoftware.com/docs/AtmosphericCorrection.html#empirical_line_calibration

Envi (2024b). Vegetation indices. Retrieved from https://www.nv5geospatialsoftware.com/docs/vegetationindices.html

Eon, R. S., & Bachmann, C. M. (2021). Mapping barrier island soil moisture using a radiative transfer model of hyperspectral imagery from an unmanned aerial system. *Scientific Reports*, *11*(1), 1–11. https://doi.org/10.1038/s41598-021-82783-3

Eon, R. S., Goldsmith, S., Bachmann, C. M., Tyler, A. C., Lapszynski, C. S., Badura, G. P., et al. (2019). Retrieval of salt marsh above-ground biomass from high-spatial resolution hyperspectral imagery using prosail. *Remote Sensing*, *11*(11), 1385. https://doi.org/10.3390/rs11111385

Ezenne, G., Jupp, L., Mantel, S., & Tanner, J. (2019). Current and potential capabilities of uas for crop water productivity in precision agriculture. *Agricultural Water Management*, *218*, 158–164. https://doi.org/10.1016/j.agwat.2019.03.034

Fourty, T., Baret, F., Jacquemoud, S., Schmuck, G., & Verdebout, J. (1996). Leaf optical properties with explicit description of its biochemical composition: Direct and inverse problems. *Remote Sensing of Environment*, *56*(2), 104–117. https://doi.org/10.1016/0034-4257(95)00234-0

Friedman, J. H. (2001). Greedy function approximation: A gradient boosting machine. *Annals of Statistics*, *29*(5), 1189–1232. https://doi.org/10.1214/aos/1013203451

Gamon, J., Serrano, L., & Surfus, J. (1997). The photochemical reflectance index: An optical indicator of photosynthetic radiation use efficiency across species, functional types, and nutrient levels. *Oecologia*, *112*(4), 492–501. https://doi.org/10.1007/s004420050337

Gamon, J., & Surfus, J. (1999). Assessing leaf pigment content and activity with a reflectometer. *New Phytologist*, *143*(1), 105–117. https://doi.org/10.1046/j.1469-8137.1999.00424.x

Gao, B.-C. (1995). Normalized difference water index for remote sensing of vegetation liquid water from space. *Imaging spectrometry*, *2480*, 225–236.

Gholizadeh, A., Žižala, D., Saberioon, M., & Borvka, L. (2018). Soil organic carbon and texture retrieving and mapping using proximal, airborne and sentinel-2 spectral imaging. *Remote Sensing of Environment*, *218*, 89–103. https://doi.org/10.1016/j.rse.2018.09.015

Gitelson, A., & Merzlyak, M. N. (1994). Spectral reflectance changes associated with autumn senescence of Aesculus hippocastanum L. and acer Platanoides L. leaves. spectral features and relation to chlorophyll estimation. *Journal of Plant Physiology*, *143*(3), 286–292. https://doi.org/10.1016/s0176-1617(11)81633-0

Gitelson, A. A., Merzlyak, M. N., & Chivkunova, O. B. (2001). Optical properties and nondestructive estimation of anthocyanin content in plant leaves. *Photochemistry and Photobiology*, *74*(1), 38–45. https://doi.org/10.1562/0031-8655(2001)074<0038:opaneo>2.0.co;2

Gitelson, A. A., Zur, Y., Chivkunova, O. B., & Merzlyak, M. N. (2002). Assessing carotenoid content in plant leaves with reflectance spectroscopy. *Photochemistry and Photobiology*, *75*(3), 272–281. https://doi.org/10.1562/0031-8655(2002)075<0272:accipl>2.0.co;2

Goldsmith, S. B., Eon, R. S., Lapszynski, C. S., Badura, G. P., Osgood, D. T., Bachmann, C. M., & Tyler, A. C. (2020). Assessing salt marsh vulnerability using high-resolution hyperspectral imagery. *Remote Sensing*, *12*(18), 2938. https://doi.org/10.3390/rs12182938

Gomez, C., Rossel, R. A. V., & McBratney, A. B. (2008). Soil organic carbon prediction by hyperspectral remote sensing and field vis-NIR spectroscopy: An Australian case study. *Geoderma (Amsterdam)*, *146*(3–4), 403–411. https://doi.org/10.1016/j.geoderma.2008.06.011

Hayden, B. P., Dueser, R. D., Callahan, J. T., & Shugart, H. H. (1991). Long-term research at the Virginia coast reserve. *BioScience*, *41*(5), 310–318. https://doi.org/10.2307/1311584

Heiri, O., Lotter, A. F., & Lemcke, G. (2001). Loss on ignition as a method for estimating organic and carbonate content in sediments: Reproducibility and comparability of results. *Journal of Paleolimnology*, *25*, 101–110.

Huete, A., Didan, K., Miura, T., Rodriguez, E. P., Gao, X., & Ferreira, L. G. (2002). Overview of the radiometric and biophysical performance of the MODIS vegetation indices. *Remote Sensing of Environment*, *83*(1–2), 195–213. https://doi.org/10.1016/s0034-4257(02)00096-2

Hunt, E. R., Daughtry, C. S., Mirsky, S. B., & Hively, W. D. (2014). Remote sensing with simulated unmanned aircraft imagery for precision agriculture applications. *Ieee Journal of Selected Topics in Applied Earth Observations and Remote Sensing*, *7*(11), 4566–4571. https://doi.org/10.1109/jstars.2014.2317876

Hunt Jr, E. R., & Rock, B. N. (1989). Detection of changes in leaf water content using near-and middle-infrared reflectances. *Remote Sensing of Environment*, *30*(1), 43–54. https://doi.org/10.1016/0034-4257(89)90046-1

Hyperspectral and operational software. (2024). Retrieved from https://www.headwallphotonics.com/products/software

Jackson, T. J., Chen, D., Cosh, M., Li, F., Anderson, M., Walthall, C., & Hunt, E. R. (2004). Vegetation water content mapping using landsat data derived normalized difference water index for corn and soybeans. *Remote Sensing of Environment*, *92*(4), 475–482. https://doi.org/10.1016/j.rse.2003.10.021

Jobbágy, E. G., & Jackson, R. B. (2000). The vertical distribution of soil organic carbon and its relation to climate and vegetation. *Ecological Applications*, *10*(2), 423–436. https://doi.org/10.2307/2641104

Kaputa, D. S., Bauch, T., Roberts, C., McKeown, D., Foote, M., & Salvaggio, C. (2019). Mx-1: A new multi-modal remote sensing UAS payload with high accuracy GPS and IMU. In *2019 ieee systems and technologies for remote sensing applications through unmanned aerial systems (stratus)* (pp. 1–4).

Karami, A., Homaee, M., Afzalinia, S., Ruhipour, H., & Basirat, S. (2012). Organic resource management: Impacts on soil aggregate stability and other soil physico-chemical properties. *Agriculture, Ecosystems and Environment*, *148*, 22–28. https://doi.org/10.1016/j.agee.2011.10.021

Kaufman, Y. J., & Tanre, D. (1992). Atmospherically resistant vegetation index (ARVI) for EOS-MODIS. *IEEE Transactions on Geoscience and Remote Sensing*, *30*(2), 261–270. https://doi.org/10.1109/36.134076

Kisi, O., Shiri, J., & Tombul, M. (2013). Modeling rainfall-runoff process using soft computing techniques. *Computers and Geosciences*, *51*, 108–117. https://doi.org/10.1016/j.cageo.2012.07.001

Klemas, V., & Smart, R. (1983). The influence of soil salinity, growth form, and leaf moisture on-the spectral radiance of. *Photogrammetric Engineering & Remote Sensing*, *49*, 77–83.

Lee, C. H., Bachmann, C. M., Nur, N. B., Mao, Y., Conran, D. N., & Bauch, T. D. (2024). A comprehensive BRF model for Spectralon® and application to hyperspectral field imagery. *IEEE Transactions on Geoscience and Remote Sensing*, *62*, 1–16. https://doi.org/10.1109/TGRS.2024.3361392

Leghari, S. J., Wahocho, N. A., Laghari, G. M., HafeezLaghari, A., MustafaBhabhan, G., HussainTalpur, K., et al. (2016). Role of nitrogen for plant growth and development: A review. *Advances in Environmental Biology*, *10*(9), 209–219.

Lobell, D. B., & Asner, G. P. (2004). Hyperion studies of crop stress in Mexico. In *Proceedings of the 12th jpl airborne earth science workshop*.

Mahmud, A., Luotamo, M., Karhu, K., Pellikka, P., Tuure, J., & Heiskanen, J. (2024). Comparison of field and imaging spectroscopy to optimize soil organic carbon and nitrogen estimation in field laboratory conditions. *Catena (Cremlingen)*, *243*, 108180. https://doi.org/10.1016/j.catena.2024.108180

McBratney, A. B., Santos, M. M., & Minasny, B. (2003). On digital soil mapping. *Geoderma (Amsterdam)*, *117*(1–2), 3–52.

McLoughlin, S. M., Wiberg, P. L., Safak, I., & McGlathery, K. J. (2015). Rates and forcing of marsh edge erosion in a shallow coastal bay. *Estuaries and Coasts*, *38*(2), 620–638. https://doi.org/10.1007/s12237-014-9841-2

Melillo, J. M., Aber, J. D., & Muratore, J. F. (1982). Nitrogen and lignin control of hardwood leaf litter decomposition dynamics. *Ecology*, *63*(3), 621–626. https://doi.org/10.2307/1936780

Merzlyak, M. N., Gitelson, A. A., Chivkunova, O. B., & Rakitin, V. Y. (1999). Non-destructive optical detection of pigment changes during leaf senescence and fruit ripening. *Physiologia Plantarum*, *106*(1), 135–141. https://doi.org/10.1034/j.1399-3054.1999.106119.x

Minasny, B., & McBratney, A. B. (2016). Digital soil mapping: A brief history and some lessons. *Geoderma (Amsterdam)*, *264*, 301–311. https://doi.org/10.1016/j.geoderma.2015.07.017

Monsalve, M. O., Cerón-Muñoz, M., Galeano-Vasco, L., & Medina-Sierra, M. (2023). Use of machine learning models for prediction of organic carbon and nitrogen in soil from hyperspectral imagery in laboratory. *Journal of Spectroscopy*, *2023*(1), 4389885.

Natekin, A., & Knoll, A. (2013). Gradient boosting machines, a tutorial. *Frontiers in Neurorobotics*, *7*, 21. https://doi.org/10.3389/fnbot.2013.00021

Nur, N. B. (2025). "Supporting data and code for "mapping soil organic matter, total carbon, and total nitrogen in salt marshes using UAS-based hyperspectral imaging. *Zenodo*. https://doi.org/10.5281/zenodo.14994443

Nur, N. B., & Bachmann, C. M. (2023). Comparison of soil moisture content retrieval models utilizing hyperspectral goniometer data and hyperspectral imagery from an unmanned aerial system. *Journal of Geophysical Research: Biogeosciences*, *128*(6), e2023JG007381. https://doi.org/10.1029/2023jg007381

Nur, N. B., Bachmann, C. M., & Bauch, T. D. (2023). A comparative study evaluating and enhancing soil moisture retrieval models for hyperspectral missions. *Agu fall meeting abstracts*, *2023*. GC53B–07.

Nur, N. B., Miller, A., Eaton, K. E., Fleck, L. G., Union, K. E., Bachmann, C. M., et al. (2023). Utilizing UAS hyperspectral imagery for precise soil organic matter, carbon, and nitrogen assessment. *AGU fall meeting abstracts*, *2023*, EP33D–2147.

Nur, N. B., Union, K. E., Miller, A., Bachmann, C. M., & Tyler, A. C. (2022). Retrieval of soil organic carbon from hyperspectral imagery. *AGU fall meeting abstracts*, *2022*. GC35A–03.

Nv5 envi 6.0. (2024). Retrieved from https://www.nv5geospatialsoftware.com/Products/ENVI

Osgood, D. T., & Zieman, J. C. (1993). Spatial and temporal patterns of substrate physicochemical parameters in different-aged barrier island marshes. Estuarine. *Coastal and Shelf Science*, *37*(4), 421–436. https://doi.org/10.1006/ecss.1993.1065

Padró, J.-C., Carabassa, V., Balagué, J., Brotons, L., Alcañiz, J. M., & Pons, X. (2019). Monitoring opencast mine restorations using unmanned aerial system (UAS) imagery. *The Science of the Total Environment*, *657*, 1602–1614. https://doi.org/10.1016/j.scitotenv.2018.12.156

Palace, M., Herrick, C., DelGreco, J., Finnell, D., Garnello, A. J., McCalley, C., et al. (2018). Determining subarctic peatland vegetation using an unmanned aerial system (UAS). *Remote Sensing*, *10*(9), 1498. https://doi.org/10.3390/rs10091498

Penuelas, J., Baret, F., & Filella, I. (1995). Semi-empirical indices to assess carotenoids/chlorophyll a ratio from leaf spectral reflectance. *Photosynthetica*, *31*(2), 221–230.

Peñuelas, J., Filella, I., Biel, C., Serrano, L., & Save, R. (1993). The reflectance at the 950–970 nm region as an indicator of plant water status. *International Journal of Remote Sensing*, *14*(10), 1887–1905. https://doi.org/10.1080/01431169308954010

Peñuelas, J., Filella, I., & Gamon, J. A. (1995). Assessment of photosynthetic radiation-use efficiency with spectral reflectance. *New Phytologist*, *131*(3), 291–296. https://doi.org/10.1111/j.1469-8137.1995.tb03064.x

Rakha, T., & Gorodetsky, A. (2018). Review of unmanned aerial system (UAS) applications in the built environment: Towards automated building inspection procedures using drones. *Automation in Construction*, *93*, 252–264. https://doi.org/10.1016/j.autcon.2018.05.002

Rossel, R. V., Walvoort, D., McBratney, A., Janik, L. J., & Skjemstad, J. (2006). Visible, near infrared, mid infrared or combined diffuse reflectance spectroscopy for simultaneous assessment of various soil properties. *Geoderma (Amsterdam)*, *131*(1–2), 59–75. https://doi.org/10.1016/j.geoderma.2005.03.007

Rouse, J. W., Haas, R. H., Schell, J. A., & Deering, D. W. (1974). Monitoring vegetation systems in the great plains with erts. *NASA Special Publication*, *351*(1), 309.

Saif, M. S., Chancia, R., Pethybridge, S., Murphy, S. P., Hassanzadeh, A., & van Aardt, J. (2023). Forecasting table beet root yield using spectral and textural features from hyperspectral UAS imagery. *Remote Sensing*, *15*(3), 794. https://doi.org/10.3390/rs15030794

Savitzky, A., & Golay, M. J. (1964). Smoothing and differentiation of data by simplified least squares procedures. *Analytical Chemistry*, *36*(8), 1627–1639. https://doi.org/10.1021/ac60214a047

Schafer, R. W. (2011). What is a savitzky-golay filter?[lecture notes]. *IEEE Signal Processing Magazine*, *28*(4), 111–117. https://doi.org/10.1109/msp.2011.941097

Serrano, L., Penuelas, J., & Ustin, S. L. (2002). Remote sensing of nitrogen and lignin in Mediterranean vegetation from AVIRIS data: Decomposing biochemical from structural signals. *Remote Sensing of Environment*, *81*(2–3), 355–364. https://doi.org/10.1016/s0034-4257(02)00011-1

Shafian, S., Rajan, N., Schnell, R., Bagavathiannan, M., Valasek, J., Shi, Y., & Olsenholler, J. (2018). Unmanned aerial systems-based remote sensing for monitoring sorghum growth and development. *PLoS One*, *13*(5), e0196605. https://doi.org/10.1371/journal.pone.0196605

Shepherd, K. D., & Walsh, M. G. (2002). Development of reflectance spectral libraries for characterization of soil properties. *Soil Science Society of America Journal*, *66*(3), 988–998. https://doi.org/10.2136/sssaj2002.0988

Shukla, A., & Karki, H. (2016). Application of robotics in onshore oil and gas industry—A review part I. *Robotics and Autonomous Systems*, *75*, 490–507. https://doi.org/10.1016/j.robot.2015.09.012

Sims, D. A., & Gamon, J. A. (2002). Relationships between leaf pigment content and spectral reflectance across a wide range of species, leaf structures and developmental stages. *Remote Sensing of Environment*, *81*(2–3), 337–354. https://doi.org/10.1016/s0034-4257(02)00010-x

Smith, D. D., Heaton, A. F., Ramazani, S., Tyler, D. A., Johnson, L., Bachmann, C., et al. (2023). Optical performance of reflectivity control devices for solar sail applications. In *Optical modeling and performance predictions xiii*.PC1266405

Stewart, J. Q. (1962). The great Atlantic coast tides of 5–8 march 1962. *Weatherwise*, *15*(3), 117–120. https://doi.org/10.1080/00431672.1962.9941001

Sun, W., Liu, S., Zhang, X., & Li, Y. (2022). Estimation of soil organic matter content using selected spectral subset of hyperspectral data. *Geoderma (Amsterdam)*, *409*, 115653. https://doi.org/10.1016/j.geoderma.2021.115653

Tyler, A. C., Lambrinos, J. G., & Grosholz, E. D. (2007). Nitrogen inputs promote the spread of an invasive marsh grass. *Ecological Applications*, *17*(7), 1886–1898. https://doi.org/10.1890/06-0822.1

Tyler, A. C., Mastronicola, T. A., & McGlathery, K. J. (2003). Nitrogen fixation and nitrogen limitation of primary production along a natural marsh chronosequence. *Oecologia*, *136*(3), 431–438. https://doi.org/10.1007/s00442-003-1277-5

Tyler, A. C., & Zieman, J. C. (1999). Patterns of development in the creekbank region of a barrier island Spartina alterniflora marsh. *Marine Ecology Progress Series*, *180*, 161–177. https://doi.org/10.3354/meps180161

Valiela, I., Chenoweth, K., Lloret, J., Teal, J., Howes, B., & Toner, D. G. (2023). Salt marsh vegetation change during a half-century of experimental nutrient addition and climate-driven controls in Great Sippewissett Marsh. *Science of the Total Environment*, *867*, 161546. https://doi.org/10.1016/j.scitotenv.2023.161546

Valiela, I., Teal, J. M., & Deuser, W. G. (1978). The nature of growth forms in the salt marsh grass Spartina Alterniflora. Source. *The American Naturalist*, *112*(985), 461–470. https://doi.org/10.1086/283290

Van Wesemael, B., Chabrillat, S., & Wilken, F. (2021). High-spectral resolution remote sensing of soil organic carbon dynamics. *Remote Sensing*, *13*(7), 1293. https://doi.org/10.3390/rs13071293

Vaudour, E., Gomez, C., Loiseau, T., Baghdadi, N., Loubet, B., Arrouays, D., et al. (2019). The impact of acquisition date on the prediction performance of topsoil organic carbon from sentinel-2 for croplands. *Remote Sensing*, *11*(18), 2143. https://doi.org/10.3390/rs11182143

Virginia Coast Reserve Long-Term Ecological Research. (2025). Virginia Coast Reserve LTER site. Retrieved from https://www.vcrlter.virginia.edu/home2/

Vogelmann, J., Rock, B., & Moss, D. (1993). Red edge spectral measurements from sugar maple leaves. *TitleREMOTE SENSING*, *14*(8), 1563–1575. https://doi.org/10.1080/01431169308953986

Walsh, J. P. (1998). *Low marsh succession along an over-wash salt marsh chronosequence*. University of Virginia.

Wolpert, D. H. (1992). Stacked generalization. *Neural Networks*, *5*(2), 241–259. https://doi.org/10.1016/s0893-6080(05)80023-1

Xu, Y., Tan, Y., Abd-Elrahman, A., Fan, T., & Wang, Q. (2023). Incorporation of fused remote sensing imagery to enhance soil organic carbon spatial prediction in an agricultural area in yellow river basin, China. *Remote Sensing*, *15*(8), 2017. https://doi.org/10.3390/rs15082017

Yang, C., Feng, M., Song, L., Wang, C., Yang, W., Xie, Y., et al. (2021). Study on hyperspectral estimation model of soil organic carbon content in the wheat field under different water treatments. *Scientific Reports*, *11*(1), 18582. https://doi.org/10.1038/s41598-021-98143-0

Young, D. R., Porter, J. H., Bachmann, C. M., Shao, G., Fusina, R. A., Bowles, J. H., et al. (2007). Cross-scale patterns in shrub thicket dynamics in the Virginia barrier complex. *Ecosystems (New York)*, *10*(5), 854–863. https://doi.org/10.1007/s10021-007-9084-1

Zhou, T., Geng, Y., Ji, C., Xu, X., Wang, H., Pan, J., et al. (2021). Prediction of soil organic carbon and the c: N ratio on a national scale using machine learning and satellite data: A comparison between sentinel-2, sentinel-3 and landsat-8 images. *Science of the Total Environment*, *755*, 142661. https://doi.org/10.1016/j.scitotenv.2020.142661

Žížala, D., Minařík, R., & Zádorová, T. (2019). Soil organic carbon mapping using multispectral remote sensing data: Prediction ability of data with different spatial and spectral resolutions. *Remote Sensing*, *11*(24), 2947. https://doi.org/10.3390/rs11242947

Zou, H., & Hastie, T. (2005). Regularization and variable selection via the elastic net. *Journal of the Royal Statistical Society–Series B: Statistical Methodology*, *67*(2), 301–320. https://doi.org/10.1111/j.1467-9868.2005.00503.x